Identification of Druggable Binding Sites and Small Molecules as Modulators of TMC1

Pedro De-la-Torre[1,*,†,&], Claudia Martínez-García[2,†], Paul Gratias[1,†], Matthew Mun[1], Paula Santana[3], Nurunisa Akyuz[4], Wendy González[5], Artur A. Indzhykulian[1,*], David Ramírez[2,*].

Affiliations:

[1]Department of Otolaryngology - Head and Neck Surgery, Harvard Medical School and Mass Eye and Ear, Boston, MA, USA

[2]Departamento de Farmacología, Facultad de Ciencias Biológicas, Universidad de Concepción, Chile.

[3]Facultad de Ingeniería, Instituto de Ciencias Químicas Aplicadas, Universidad Autónoma de Chile, Santiago, Chile.

[4]Department of Neurobiology, Harvard Medical School, Boston, MA, USA

[5]Center for Bioinformatics and Molecular Simulations (CBSM), University of Talca, Talca 3460000, Chile

[*]Correspondence should be addressed to:

dramirezs@udec.cl,

inartur@hms.harvard.edu,

pedro_delatorremarquez@meei.harvard.edu

[†]These authors contributed equally to this work

[&]Current address:

Facultad de Ciencias Básicas; Universidad del Atlántico; Barranquilla, Colombia.

Life Sciences Research Center, Universidad Simón Bolívar, Barranquilla, Colombia

ABSTRACT

Our ability to hear and maintain balance relies on the proper functioning of inner ear sensory hair cells, which translate mechanical stimuli into electrical signals via mechano-electrical transducer (MET) channels, composed of TMC1/2 proteins. However, the therapeutic use of ototoxic drugs, such as aminoglycosides and cisplatin, which can enter hair cells through MET channels, often leads to profound auditory and vestibular dysfunction. Despite extensive research on otoprotective compounds targeting MET channels, our understanding of how small-molecule modulators interact with these channels remains limited, hampering the discovery of novel drugs. Here, we propose a structure-based screening approach, integrating 3D-pharmacophore modeling, molecular dynamics simulations of the TMC1+CIB2+TMIE complex, and experimental validation. Our pipeline successfully identified several novel compounds and FDA-approved drugs that reduced dye uptake in cultured cochlear explants, indicating MET-modulation activity. Simulations, molecular docking and free-energy estimations allowed us to identify three potential drug-binding sites within the channel pore, phospholipids, key amino acids involved in modulator interactions, and TMIE as a flexible component of the MET complex. We also identified shared ligand-binding features between TMC and structurally related TMEM16 proteins, providing novel insights into their distinct inhibition. Our pipeline offers a broad application for discovering modulators for mechanosensitive ion channels.

INTRODUCTION

The sensory hair cells of the inner ear function as mechanoreceptors, converting various mechanical stimuli—including sound-induced vibrations, gravitational forces, and linear acceleration—into electrical signals, mediating our senses of hearing and balance. However, deficiencies or malfunctions in hair cells, stemming from genetic mutations[1,2], aging[3], exposure to loud noise[4], or drug-induced ototoxicity, often result in hearing loss. Notably, platinum-containing chemotherapeutic drugs[5,6] and the aminoglycoside (AG) group of antibiotics are known ototoxic agents that cause hearing loss and balance dysfunction[5,7].

Recent studies suggest that non-AG antibiotics may also cause ototoxicity, although clinical reports of such cases are less frequent[8]. AG ototoxicity may occur due to several factors, including the administration of doses exceeding the therapeutic range, or the use of enantiomeric mixtures of AG[9]. Several mechanisms have been implicated in AG-induced hearing loss[10–15]. It is widely recognized that AG uptake into hair cells primarily occurs through the mechanoelectrical transduction (MET) channels, a protein complex formed between the pore-forming TMC1/2 subunits[16–20], and other binding partners such as TMHS, CIB2, and TMIE[21]. Surprisingly, about 9000 dihydrostreptomycin (DHS) molecules per second are predicted to enter into hair cells in a voltage-dependent manner[22], at therapeutic concentrations[17].

MET channels are gated by force transmitted through tip-link filaments[23,24] composed of cadherin-23 (CDH23)[25,26] and protocadherin-15 (PCDH15)[27–31], also members of the MET complex. The resting tension applied by the tip link to the MET channel results in an increased open probability of MET channels at rest, enabling AG uptake[31,32]. Consequently, disruption of tip links by calcium (Ca^{2+}) chelators closes the MET channel, preventing AG uptake into hair cells[20]. These findings inspired numerous studies aimed at identifying MET channel blockers for use as otoprotective compounds, predating the identification of molecules that form the MET channel complex[19,33–38]. The identification of TMC1 as the pore-forming channel subunit has opened up new venues of research for identifying novel pharmacological agents capable of reversibly blocking the MET channel.

Similar to AG treatment, cisplatin causes permanent hearing loss in a significant portion of treated patients, due to its gradual accumulation in the cochlea over months to years[39]. Given the impact caused by ototoxic side effects of both AG and cisplatin, the pursuit for identification of novel drugs to prevent the resulting hearing loss is ongoing[33–35,40–42]. Currently, there are at least 17 clinical trials evaluating 10 different therapeutics to prevent aminoglycoside and/or cisplatin-induced ototoxicity[43]. Recently, the Food and Drug Administration (FDA) approved sodium thiosulfate (STS) to reduce the risk of cisplatin-induced ototoxicity in pediatric patients[44,45], although its mechanism of action is not fully understood[46]. Studies using animal models, however, suggest that STS does not protect hair cells against AG-induced cell death[47], and it remains unclear whether STS interacts with the MET channel[48–52]. This underscores the need for structure-guided search for novel otoprotectants to mitigate ototoxicity mediated by the MET channel in order to prevent hearing loss in children and adults.

Multiple studies have focused on designing or structurally modifying small molecules to serve as potential otoprotectants against AG-induced hair-cell loss[19,33–36,42,53,54]. However, their interactions within the TMC1 pore remain largely unknown, and whether these compounds share any common TMC1-binding mechanisms is not well understood[17,18,55–59]. A previously reported molecule screen using a chemical library of 10,240 compounds, identified UoS-7692 and several others as potent MET blocker[33] (**Figure 1**). This compound demonstrated strong otoprotection against AG in zebrafish larval hair cells and in mouse cochlear explants[33].

While experimental screening of relatively small libraries of compounds typically focuses on their *in vitro* and *in vivo* evaluation in hair cell-like cell lines, live zebrafish larvae or in mouse cochlear explants, this laborious and a relatively low-throughput approach limits exploration of the broad chemical space. Interestingly, no *in silico* data evaluating binding modes of known MET channel blockers within the TMC1 pore cavity has been reported to date. Therefore, conducting an *in silico* screen to evaluate the binding of potential MET channel blockers to TMC1, followed by more conventional *in vitro* experiments to confirm the *in silico* predictions, is an attractive strategy for discovering novel TMC1 modulators.

The pharmacophore concept, defined as the set of structural features recognized at a receptor site or derived from the structure of a ligand, plays a crucial role in determining the bioactivity of a molecule[60,61], and serves as a valuable tool in drug discovery. However, the application of a ligand-base pharmacophore concept for discovering novel TMC1 modulators remains largely unexplored in the context of drug discovery, and the 3D-pharmacophoric and structural factors involved in TMC1-ligand interactions are not well understood. Given the structural diversity of compounds reported as potential MET channel blockers[19,33–38,54] (**Figure 1**), conducting a comprehensive study to analyze their shared ligand-based pharmacophoric features and their binding to TMC1 is essential to identifying or developing potent and selective MET channel modulators that could potentially serve as otoprotectants. Conversely, considering that TMC1 proteins share structural and sequence similarities with the TMEM16 and OSCA families of membrane proteins[18,55,62–65], potential ligand-based pharmacophores from molecules that modulate their function could also be employed to explore the polypharmacology of these related proteins.

In silico pharmacophore modeling[66–69], molecular docking[70–77], and binding free energy[78–80] studies have emerged as powerful methods for discovering bioactive small molecules. These methods enable a deeper understanding of the key structural factors and moieties required for hit-to-lead optimization with improved biological activities. Previously, we have successfully utilized these methods to design blockers for several ion channels as well as to design other small molecules of biological relevance[81–84].

In this study, we devised a versatile computational strategy to explore the binding modes of known TMC1 blockers and to identify novel modulators of TMC1. Our strategy combines *in silico* modeling with experimental validation of compounds in mouse cochlear explants. First, we developed common 3D-ligand-based pharmacophore models for small molecules based on known MET channel blockers and predicted their binding modes within the TMC1 druggable pore. These models enabled us to pre-select 258 candidate compounds from over ~22 million compounds (representing ~220 million conformers), sourced from two distinct chemical libraries (non-FDA-approved and FDA-approved drugs).

Using *AlphaFold2*-based structural predictions[72] of the TMC1 protein in an open-like state[85], we conducted a virtual screening (VS) of these 258 molecules, to predict their potential binding modes. Furthermore, we compared 3D-pharmacophore features of TMC1 blockers with compounds modulating the activity of the paralog TMEM16A protein, to identify potential structure-pharmacophoric relationships.

We then assessed the binding energies of the docking poses by predicting their binding-free energies using molecular mechanics with generalized Born and surface area (MM/GBSA)[86] methods. From each library, we selected the top 10 hits based on their predicted binding energies and structural diversity for subsequent *in vitro* evaluation, ensuring their commercial availability for experimental testing. Next, the MET blocking capacity of each hit candidate was evaluated *in vitro* using the AM1-43[56] dye uptake assay in mouse cochlear explants using live microscopy imaging. AM1-43, developed as a fixable analogue of FM1-43, functions in live tissue similar to FM1-43, and is often used for both, live and fixed tissue imaging. Our screening pipeline successfully identified hit compounds that demonstrated a reduction of AM1-43 uptake in cochlear hair cells (**Supp Figure 1)**.

In summary, we developed and experimentally validated, for the first time, a set of effective 3D-pharmacophore models and successfully utilized them to identify novel families of MET channel modulators. We then predicted the binding of these compounds within the pore of the TMC1 channel and presented a list of potential binding sites for both known and newly discovered modulators. This structural modeling approach, including molecular dynamics (MD) simulations involving TMC1, CIB2, and TMIE proteins, combined with experimental evaluation in hair cells, allowed us to reveal new putative binding sites critical for ligand interaction within the TMC1 pore. Our *in silico* approach also predicted flexible properties for TMIE in the MET complex, as well as potential shared pharmacophoric properties between small molecules reported to interact with both TMC1 and TMEM16A proteins[87].

RESULTS

Building a good-quality structural model of TMC1 for virtual screening

Homology and experimental structural models for TMC1 and TMC2 have contributed to identifying a putative pore and providing insights into the ion permeation pathway[18,64,85,88]. Cryo-electron microscopy (Cryo-EM) structures of *C. elegans* (*Ce*) TMC1 have confirmed, at atomic resolution, structural similarities between TMCs and TMEM16, as well as the TMEM63/OSCA protein families[55,62,64,89]. Specifically, TMC1 assembles as a dimer with 10 transmembrane (TM) domains per subunit, similar to TMEM16 proteins[64], while OSCA channels have an additional TM domain, totaling 11 per subunit[65].

In the absence of 3D-atomic structures of the mammalian MET-channel complex, we constructed a model of the complex by assembling *Mus musculus* (*Mm*) TMC1 subunits with *Mm*CIB2 and *Mm*TMIE. *Mm*CIB2 was included to increase the stability of the MET complex and preserve its influence in phospholipid dynamics and ion permeation[21,90]. We utilized the Cryo-EM structure of the expanded *Ce*TMC-1 complex (PDB ID: 7USW)[55] as a reference for structural alignment, and employed the *AlphaFold2* and *Maestro* software[91] for structural modeling. The assembled complex was compared to the *Ce*TMC-1 cryo-EM structure, confirming that the TM10 domain adopted the characteristic domain-swapped conformation[55], which is a structural requirement for the proper oligomerization of *Mm*TMC1 (**Figures 1-2**). Since some previous reported TMC1 simulations do not include TMIE[21,90], we decided to introduce this component[55] in our modeled mouse MET-channel complex.

Next, the model was subjected to energy minimization, followed by embedding into a pre-equilibrated 1-palmitoyl-2-oleoyl-sn-glycero-3-phosphocholine (POPC) phospholipid membrane and solvation with a final ionic concentration of 0.15 M KCl (**Figure 2**) (See *Methods*). Subsequently, the system underwent 25 ns of restrained MD simulation. The Root Mean Square Deviation (RMSD), which measures global structural changes across all backbone atoms, was monitored to assess conformational stability. Equilibration was achieved after 2 ns of MDs, and the RMSD of all backbone atoms remained within 2 Å distance for the entire complex throughout the remaining simulation time (**Supp Figure 2A**), indicating stable conformation of the modeled structure.

When analyzing hetero-subunits independently, no major changes were observed along the 25 ns trajectory, which is in agreement with the literature for MDs of membrane proteins[92–94]. Both TMC1 and CIB2 protomers remained stable during the 25 ns MDs, with RMSD values at ~2 Å. Some fluctuations were also observed in the C-terminal TMIE domain, with RMSD values within 4 Å along the trajectory. This behavior was likely attributable to the “elbow-like” linker[55] as a new flexible component of the MET complex, allowing for the TMIE cytoplasmic helix to move more freely (**Figure 2C**, and **Supp Figure 2A**).

Root Mean Square Fluctuation (RMSF) analysis, which assesses local atomic fluctuations and flexibility, revealed that TMC1 chains exhibited fluctuations under 2 Å, similar to its paralog TMEM16A[95] (**Supp Figure 2C**). Even though TMIE has limited interactions with TMC1, its single pass N-terminal TM domain fragment presented low fluctuations, likely because it is embedded within the bilayer membrane (**Figure 2C** and **Supp Figure 2C**). In contrast, the C-terminal cytoplasmic helix of TMIE displayed larger fluctuations, likely because it is positioned outside the bilayer membrane and is exposed to solvent, hinging about a flexible region (**Figure 2C** and **Supp Figure 2C**). Similarly, the CIB2 protomers displayed comparable RMSF fluctuations in their N-terminal domains, likely due to the random-coil configuration of these regions (**Supp Figure 2C**).

The spatial distribution of atoms within the MET complex was assessed using the radius of gyration (*Rg*) measurements (**Supp Figure 2B**), and no major changes were detected, with *Rg* values remaining within 1 Å consistent with reports from other 100 ns simulations of membrane proteins. Thus, our results align with previously reported MD simulations of membrane proteins[92–94,96]. To further ensure that the stability of the MET complex was indeed achieved within 25 ns, we extended the simulation to 100 ns under identical MD conditions, revealing no major structural changes (**Supp Figure 2D-F**). This stability can be attributed, in part, to the constraints applied during the simulation, ensuring the stability of the ion channel, and resulting in minimal, if any, conformational differences within the TMC1 protomers and its pores during

25 ns vs 100 ns simulation periods (**Supp Figure 2G-J**). Notably, our HOLE[97] analysis demonstrated that the calculated average pore radius (± standard deviation) remained consistent, with no major changes in the pore size distribution. This was assessed at 1 nanosecond intervals for the pore of chain A, and compared across the 25 ns and 100 ns trajectories **(Supp Figure 2H).**

During the 25 ns MD simulations, various phospholipids were observed migrating into the pore, positioning their polar heads near the top and the bottom of the putative TMC1 pore cavity, with their hydrophobic tails directed towards the pore (**Figure 2F**, and **Figures 4C, 4G-I**). These lipid movements along the trajectory agree with the findings reported in the literature[55,90], where phospholipids were suggested to move dynamically between the TM4 and TM6 domains of TMC1[21,90], providing further insights into the structural dynamics and lipid-protein interactions within the TMC1 pore.

Furthermore, our analysis revealed the presence of several water molecules and potassium (K^+) ions within the pore cavity during the MD simulation, indicating a hydrated pore (**Figure 2F**). These findings are in agreement with previous reports, which emphasize the importance of a hydrated environment in facilitating potential drug binding within the TMC1 pore[18,21,55,57,88,90], further supporting our structural model.

The combination of MD simulations and channel pore analysis by HOLE[97], has facilitated the identification of three primary target regions within the two elongated TMC1 pores (**Figure 2**). Along the *z* axis, we have assigned these regions to an expanded top site located near the extracellular region, a narrowed middle site within the transmembrane segment, and a more expanded bottom site near the intracellular region (**Figure 2B**). The target regions we identified are suitable for screening of druggable-binding sites within the pore and can facilitate a comprehensive conformational search of both known and novel TMC1 interacting molecules using molecular docking (**Figure 1**, and **Figure 2B-E**).

Identification of common pharmacophores for MET channel block.

In this study, we analyzed the chemical structures of known MET channel blockers and identified 3D-pharmacophoric features that contribute to their antagonistic activity (**Figure 1, Table 1, Supp Table 1**). These 3D elements include specific functional groups, spatial arrangements, or physicochemical properties that are essential for binding to the MET channel and modulation of its function. The 3D-pharmacophoric models were then used to screen large chemical databases to identify new candidate compounds with similar pharmacophoric features. Suitable hit compounds were then tested *in vitro*.

We used the Pharmacophore Alignment and Scoring Engine (*Phase*)[68] software, an intuitive pharmacophore modeling tool (See *Methods*) to design 3D-pharmacophore models representing the main structural features of known MET channel blockers. These 3D-pharmacophore features were extracted by assembling a training set consisting of 13 structurally diverse compounds, including UoS-7692[33], UoS-3607[33], UoS-3606[33], UoS-5247[33], UoS-962[33], Proto-1[98], E6-berbamine[54], hexamethyleneamiloride[37], amsacrine[37], phenoxybenzamine[37,99], carvedilol-derivate 13[53], ORC-13661[34,36], and FM1-43[58,59], a positively charged styryl dye often used to label hair cells and to check MET-channel function[58,59] (**Figure 1** and **Supp Table 1**).

These compounds coalesced into 10 predicted pharmacophores (**Table 1** and **Figure 3**), which were ranked based on their *PhaseHypoScore* values[68]. The top-scoring pharmacophore, designated as APRR (ID #1), achieved a *PhaseHypoScore* of 0.780. High *PhaseHypoScore* values indicate how well the pharmacophoric-feature vectors align with the structures of the compounds in the 3D-pharmacophore model (See *Methods*). All 10 3D-pharmacophores along with their matching compounds, are reported in **Supp Table 2** and **Supp Figure 3**.

The APRR pharmacophore consists of four key features: one hydrogen bond acceptor group (*A*), one positively charged group (*P*), and two aromatic rings (*R*) (**Figure 3A**). Notably, this model matched 7 out of the 13 known MET blockers reported in the literature, which we used as a training set for this study (**Table 1, Figures 3A-I,** and **Supp Table 2**). The remaining nine pharmacophores (ID #2 to #10) were modeled with three pharmacophoric features, reaching *PhaseHypoScore* values between 0.340 and 0.762 (**Table 1**).

239 Most of these pharmacophore models shared at least one common aromatic ring (R), and one acceptor
240 group (A), except for the PRR (ID #4) and HPP (ID #10) models. Furthermore, the top four
241 pharmacophores: APRR, APR-1, APR-3, and PRR (IDs #1 to #4) contained one protonatable group (P),
242 matching 7 (APRR), 9 (APR-1), 8 (APR-3), and 7 (PRR) of the 13 known MET blockers, respectively. This
243 suggests that a protonatable amine (positively charged N^+ group) is likely crucial for blocking TMC1
244 activity, consistent with experiments reported in the literature[33,53,57].

245 To validate our pharmacophore models, we tested their ability to discriminate between decoys and known
246 MET channel blockers. We evaluated the performance of the models using the area under the curve (AUC)
247 of the corresponding receiver operating characteristic (ROC) curve. The AUC value ranges from 0 to 1,
248 with 1 indicating ideal performance and 0.5 indicating random behavior. All AUC values for our models
249 ranged from 0.86 to 0.99 (**Supp Table 3**), demonstrating that our pharmacophore models can accurately
250 classify compounds as active or inactive. Additionally, all the active compounds (known MET-channel
251 blockers) were successfully identified by each pharmacophore model.

252 We further evaluated the performance of each pharmacophore using the Güner-Henry (GH) scoring
253 method. This metric is a reliable indicator, because it incorporates both the percentage ratio of active
254 compounds in the hit list and the percentage yield of active compounds in a database. The number of
255 active and decoy compounds for each pharmacophore, along with the characteristics for GH (eg,
256 sensitivity (Se), specificity (Sp), enrichment factor (EF), percentage yield of active compounds (Ya), and
257 % yield of actives (% Yield) are listed in **Supp Table 3**. Eight out of the ten pharmacophore models have
258 a GH score higher than 0.7 indicating that these models are good and reliable[100–103]. Some studies
259 consider a GH score greater than 0.5 to indicate a good model reliability[104], suggesting that
260 pharmacophores ARR-1 (GH score = 0.675) and HRR (GH score = 0.664) are also valid models.

261 ***Pharmacophore-based virtual screening of hit compounds.***

262 Next, we employed Pharmacophore-Based Virtual Screening (PBVS), a computational method for
263 screening large chemical databases to identify molecules that possess pharmacophoric features similar
264 to a reference pharmacophore model[68]. In this study, we screened for compounds that matched any of
265 the 10 pharmacophore models we developed. We used two libraries of compounds as databases: Library
266 1, which contains over 230 million commercially available, non-FDA-approved compounds (ZINC20
267 database)[105], and Library 2, which consists of 1,789 FDA-approved drugs (MicroSource Discovery
268 Systems)[106].

269 PBVS was carried out using two consecutive steps. In the first step, we used *ZINCPharmer*[107], a free
270 pharmacophore search software, to screen commercial compounds from the ZINC database[105]. The
271 second step involved the *Phase* (see *Methods*), which employs a *PhaseScreenScore* function that
272 evaluates both the quantity (partial compound matching) and quality of ligand feature matching. This
273 evaluation includes site matching, pharmacophore feature alignment, and volume-scoring components for
274 each compound[108].

275 The first step of our PBVS analysis involved inputting the 10 pharmacophore models into the
276 ZINCPharmer[107] (see **Table 1** and **Supp Figure 3**). We then selected the top 5,000 compounds with the
277 lowest RMSD, indicating a good fit to the respective pharmacophore model, resulting in a total of 50,000
278 pre-filtered compounds (5,000 compounds × 10 pharmacophore models). After pharmacophore matching
279 with ZINCPharmer, we selected only those compounds that matched with two or more pharmacophore
280 models to increase the reliability of our PBVS. This filtering resulted in 4,187 compounds from the ZINC
281 database that matched with one or more pharmacophore models (**Supp Table 4**).

282 Next, the 4,187 chemical structures were processed using the *LigPrep*[109] and *Epik*[110,111] modules of the
283 *Maestro* software[91] (See *Methods*) to structurally optimize the dataset and perform the second step of
284 PBVS with *Phase*. *LigPrep* module was used to generate 3D structures and optimize their geometry, while
285 the *Epik* module predicted up to 10 different optimized structures (i.e. conformations) per each of the 4,187
286 compounds, accounting for protonation and ionization states, tautomers, and chiralities at specific pH

levels (see *Methods*). This increased the total number to 4,501 processed molecules, including 314 additional conformational pairs, identified with different protonation or structural conformations.

Subsequently, we performed the second step of Phase-PBVS screening and calculated the highest *PhaseScreenScore* values from the 4,501 processed molecules corresponding to each of the 10 pharmacophore models. Of the 314 additional molecules that represented various confirmations of the original compounds, we selected the best *PhaseScreenScore* value across all conformations for each compound, reducing the library down to 4,187 optimized molecules **(Supp Table 4).**

The results were ranked based on their *Total-PhaseScreenScore* (TPS_S) ranging in values between 1.157 and 21.512. These values were then used to calculate the docking threshold (D_T), set to TPS_S score values above the mean plus two standard deviations (Mean + 2 SD), as a requirement for selecting compounds for final molecular docking (see *Methods,* Equation 1). Of the 4,187 optimized compounds from Library 1, many aligned with multiple pharmacophore models (**Supp Figure 4A**): 1,625 compounds matched six of the ten different pharmacophores, while 16 optimized compounds matched only two pharmacophores. After applying the D_T threshold, 207 effective compounds were selected for molecular docking to predict their binding modes (**Supp Figure 4B**).

A similar second Phase-PBVS screen was performed for compounds from Library 2 using Phase. First, the 1,789 FDA-approved drugs underwent ligand optimization (including the assignment of charges, determination of protonation states, tautomer, and chirality determination) using *LigPrep*[109] and *Epik*[110,111] modules of the *Maestro* software[91] (see *Methods*). This resulted in a total of 2,628 optimized drug molecules, including 839 additional confirmations, reflecting different protonation states, conformers, stereoisomers, and enantiomers for each compound. All 2,628 optimized drug molecules were used for PBVS to determine their *PhaseScreenScore* and TPS_S values. For the 839 additional molecules, the best *PhaseScreenScore* value was selected, reducing the library down to the 1,789 structurally optimized drug molecules (**Supp Table 5**).

Among the 1,789 structurally optimized drugs, 906 matched to one or more pharmacophore models: 332 matched one of the ten different pharmacophores, 574 aligned with two or more pharmacophores, and 26 of those optimized drugs matched all ten pharmacophores (**Supp Figure 5C**, and **Supp Table 5**). Conversely, the remaining 883 drugs were excluded by the PBVS as they did not match any pharmacophores. The TPS_S values for the matching drugs ranged between 0.419 and 18.593 (**Supp Table 5**). Subsequently, we calculated the docking threshold (D_T) values to select compounds that will pass for the next step of molecular docking, identifying 53 effective compounds (**Supp Figure 4D**). In this second step of PBVS, the optimized molecules from Library 1 exhibited higher *PhaseScreenScore* results compared to those from Library 2 (**Supp Figure 4**). This is likely because, unlike Library 1, Library 2 is smaller and was not pre-screened using *ZINCPharmer* in the first step of PBVS. In contrast to the ZINC database, the smaller size of the FDA-approved dataset made it computationally feasible to screen all compounds directly.

A closer examination of the structural features of each pharmacophore model and the matching selected compounds from Libraries 1 and 2 suggests that the best-scoring ligands adhere to three or four common point-pharmacophoric features. In Library 1, the APRR model was the highest-ranked pharmacophore model for the compound ZINC26876007, with a *PhaseScreenScore* of 2.449 (**Supp Table 4**). In Library 2, carvedilol was the highest-ranked compound, scoring best with both, the APR-1 model (*PhaseScreenScore* = 2.301) and the APRR model (*PhaseScreenScore* = 1.736) (**Supp Table 5**). The identification of carvedilol as a potential compound further validates our PBVS design, as carvedilol was previously reported as a MET channel blocker[37,53], despite not being included in our training set of compounds used to design the pharmacophores (**Supp Tables 1-2**).

Predicting binding sites of known MET blockers within the pore region of TMC1

Next, we used molecular docking and molecular mechanics with MM-GBSA methods to predict the binding sites and affinities of 16 known MET blockers within the pore region of TMC1 (See *Methods*).

335 This set included 13 blockers used in the training set for building 3D-pharmacophore models (**Figure 1,**
336 **Supp Table 1**), as well as three known potent MET blockers: benzamil[33,38,112–114], tubocurarine[19,114], and
337 DHS[17,22,115,116]. These three additional blockers are potent MET blockers but were not included in the
338 training set due to chemical similarities with other blockers, such as functional moieties found in E6-
339 berbamine and hexamethyleneamiloride (**Figure 1A**).

340 To explore the conformational space of the TMC1 pore, we performed docking simulations using our
341 modeled *open-like mm*TMC1 structure in complex with CIB2 and TMIE. We used HOLE analysis to identify
342 and characterize the pore, allowing us to precisely target the transmembrane region for docking
343 simulations (**Figure 2**). A gridbox of $41_x \times 41_y \times 41_z$ Å^3 was positioned to cover the pore region. The
344 placement of the grid box is based on solid experimental evidence indicating that the pore of TMC1 is a
345 pathway for both ion and small molecule uptake into hair cells. Thus, the grid box effectively encompassed
346 the chemical space of the TMC1 pore, making it suitable for molecular docking. Docking simulations were
347 carried out with the membrane bilayer from equilibrated 25 ns MDs. During the docking process, ligands
348 were allowed to move freely without constraints (**Figure 2**).

349 Two phospholipid molecules (referred to as POPC-A and POPC-B) were identified near the top (residues
350 R523 and N404) and the bottom (residues T416, D419, R543, and D569) regions of the pore. These
351 phospholipids were observed to enter the pore cavity and form a sidewall between TM4 and TM6 along
352 the pore region (**Figure 2F, Figure 4C**, and **Figure 5G-I**), potentially modulating the accessibility and
353 binding of small molecules with their polar and hydrophobic moieties.

354 Using the standard precision (SP) scoring function to enrich the conformational sampling of the
355 compounds within the TMC1 pore, we predicted a total of 178 docking poses for the abovementioned 16
356 MET blockers. Each blocker generated up to 10 poses, including the *R* and *S* stereoisomers for
357 tubucurarine and phenoxibenzamine. These poses were evaluated using the *Emodel* score[117] (see
358 *Methods*), which reflects the quality of each cluster of poses.

359 All compounds successfully docked in three main areas of the pore, which we have named the top, middle,
360 and bottom sites (**Figure 2B** and **Figure 4**). At the **top site**, key residues involved in binding include F451,
361 E520, R523, S527, and the phospholipid POPC-B. At the **middle site**, important residues include M407,
362 S408, M412, N447, D528, T531, T532, and R601. At the **bottom site**, key residues identified are T535,
363 D569, and the phospholipid POPC-A. A detailed list of key binding residues and their interactions with the
364 blockers, including benzamil, tubocurarine, and DHS are presented in **Supp Table 6.**

365 *FM1-43 Predictions*

366 FM1-43, a positively-charged fluorescent dye commonly used to test for functional MET channels[57–59],
367 displayed interactions across all three regions of the TMC1 cavity, particularly with residues of the TM4
368 and TM5 helices (**Figure 5A**). At the top site of the pore (depicted in *gold*), FM1-43 is positioned between
369 F451 and N404 and exhibits a 4.14 Å cation–π interaction between its positive triethylammonium group
370 and F451 (**Figure 4D** and **5A**). This group is also surrounded by the negatively charged residues E458
371 and E520, engaging in a zwitterionic-hydrogen bond network (referred to as the ZN1 site) formed by D239,
372 R523 and the polar head of POPC-B at the entrance of the pore (**Figure 5A** and **Supp Figure 5**).
373 Additionally, hydrophobic interactions with M403 and M407 further stabilize FM1-43 in this region.

374 Within the middle site of the pore (**Figure 4,** shown in *light gray*), the hydrophobic aromatic core of FM1-
375 43 interacts with the tail of POPC-B, which further stabilizes the ligand within the cavity. The benzene
376 group of FM1-43 forms close hydrophobic contacts with residues G411 (TM4), L444 (TM5), as well as
377 V574 and L575 (TM7). At the bottom of the pore (**Figure 4,** shown in *light red*), the positively charged
378 dibutylamine group is positioned near the polar head of POPC-A, pointing towards residue D569. Since
379 both the docking and MM-GBSA methods use a dielectric field to implicitly simulate water molecules, we
380 acknowledge the possibility that water molecules may participate in the binding interactions of the
381 dibutylamine group with D569 and POPC-A if simulated with explicit solvent (**Supp Figure 5**).

382 Notably, docking results predicted that the positively charged atoms of FM1-43 are located inside the pore,
383 while some structural moieties are docked outside the HOLE-pore contour, closer to the phospholipid wall.

384 This suggests that ions and ligands may follow distinct permeation pathways while sharing common key
385 amino acid residues involved in both cation and ligand binding (**Supp Figure 6**).

386 *Tubocurarine Predictions*

387 The alkaloid tubocurarine exhibited interactions at the middle and bottom sites of the pore (**Figure 4F** and
388 **4I**). Like FM1-43, tubocurarine displayed analogous interactions around the TM4, TM6, and TM7 domains
389 of TMC1. The positive dimethyl-ammonium group of the tetrahydroisoquinoline moiety is positioned near
390 residues S408 and N447, and a hydrophobic interaction was observed with residue F579 (TM7) within the
391 middle site of the pore (**Figure 5C**). The phenolic group linking the two tetrahydroisoquinoline scaffolds
392 forms a hydrogen bond with residue T535 and is in close contact (4.12 Å) with T531 on TM6. T535 is
393 adjacent to a second identified zwitterionic-interaction zone, composed by D528, T531, T532, R601, and
394 N580, which we refer to as the ZN2 site (**Supp Figure 5**).

395 In the bottom site, the protonatable amine of the second methyl-tetrahydroisoquinoline scaffold forms a
396 dual salt bridge with D569 at a distance of 4.22 Å, and a hydrogen bond with the phosphate group of
397 POPC-A at 2.82 Å, a component of a third zwitterionic-interaction network (ZN3) (**Figure 5H**). The
398 distances were measured between heavy atoms and the polar N^+ group.

399 *Benzamil Predictions*

400 Benzamil primarily engages in significant interactions at the bottom site (depicted in *light red*) of the pore
401 cavity. The amine group at position 3 of the pyrazine ring forms dual hydrogen bonds with D528 and T532
402 on TM6. These residues, along with R601 (TM8), N598, and N580 (TM7), constitute the ZN2 site, which
403 effectively clamps and stabilizes the pocket formed between TM6, TM7, and TM8 (**Figure 5B** and **Supp**
404 **Figure 5**). The 6-chloropyrazine ring is located near residue N573 (TM7) and Q609 (TM8). The N-
405 benzylcarbamimidoyl group interacts with residue M412, the site of the M412K Beethoven mutation on
406 TM4[118], as well as with the hydrophobic tail of POPC-A, forming van der Waals interactions.

407 In addition, the positively charged amidino group forms a salt bridge with D569 (2.82 Å) and a hydrogen
408 bond with the phosphate head of POPC-A (3.1 Å). This phosphate head further establishes a hydrogen
409 bond with T416, thereby expanding the ZN3 interactions at the bottom site (**Figure 5G** and **Supp Figure**
410 **5**). Our results indicate that the ZN1, ZN2, and ZN3 interaction zones play crucial roles in ligand binding
411 and TMC1 stabilization at the top (along with F451), middle, and bottom sites of the TMC1 pore,
412 respectively.

413 Notably, these zwitterionic zones contain known residues implicated in ion permeation, such as D528 and
414 D569, which are essential for ligand binding, blocking the TMC1 pore, as well as TMC1 protein
415 expression[85,119,120]. In addition, our results suggest that residues T532 and T535 are essential for hydrogen
416 bonding interactions with benzamil and tubocurarine, respectively.

417 *DHS Predictions*

418 *LigPrep* and *Epik* predicted two main charged forms of DHS, consistent with structures reported in the
419 literature[121,122]. One form, referred to as DHS 2^+, carries two positive charges due to the protonation of the
420 two guanidinium groups in the streptidine moiety (**Figure 6A-D**). The second form, DHS 3^+, has an
421 additional positive charge from the protonated *N*-methyl-*L*-glucosamine moiety (**Figure 6E-F**).

422 DHS 2^+ displayed interactions towards the middle and bottom sites of the TMC1 pore (**Figure 6B-C**). Like
423 most of the middle-site interactions analyzed above, the neutral *N*-methyl-*L*-glucosamine moiety of DHS 2^+
424 formed double hydrogen bonds with D528 on TM6, and the backbone carbonyl of S408 on TM4 at the
425 middle site. Within the bottom site, the hydroxyl and the guanidinium groups of the streptidine moiety show
426 direct interactions with N573 on TM7, D540 on TM6, and the negatively charged head of POPC-A (**Figure**
427 **6D**).
428 Similarly, DHS 3^+ displayed direct interactions with residues D528, S408, D540, N573, and the
429 phospholipid head of POPC-A. Additionally, the streptose moiety formed hydrogen bonds with the
430 backbone carbonyl groups of G411 on TM4 and G572 on TM7. One guanidinium group of the streptidine

431 pointed towards T416, forming direct interactions with the backbone carbonyl of M412 on TM4, while the
432 second guanidinium group interacted with the backbone carbonyl of E567 (**Figure 6E-F**).
433
434 Our findings propose DHS-TMC1 interactions through residues G411, G572, S408, D540, N573, and
435 E567. These newly predicted interacting residues, along with the well-characterized M412, T416, and
436 D528 interaction sites of DHS[88,115], further validate our docking predictions and provide strong confidence
437 in the predicted docking poses of other compounds studied in this work. Furthermore, our predictions also
438 suggest that phospholipids may play a key role in DHS binding. Overall, our results for DHS interaction
439 within the TMC1 pore are consistent with previously reported results obtained using *in vitro*
440 electrophysiology data[88,115], thereby reinforcing the validity of our predictions (**Figure 6**).

441 ***Phospholipid effect on ligand binding affinities in the TMC1 pore: MM-GBSA rescoring analysis.***

442 During the MD simulations, phospholipids (specifically POPC-A and POPC-B) were found to form a lipidic
443 "sidewall" between two transmembrane domains, TM4 and TM6. This close proximity to the pore raised
444 the question of whether the presence of these phospholipids influences the binding affinity of blockers to
445 the TMC1 protein.

446 To investigate this, we first re-scored the docking results using MM-GBSA to predict the binding strength
447 of the 16 MET blockers to the TMC1 protein in the absence of phospholipids. We calculated the relative
448 binding free energies (ΔG_{bind}) for the ligands (the known 16 blockers, listed in **Supp Table 7**) also using
449 MM-GBSA. We then investigated whether interactions with POPC-A and POPC-B affected the TMC1-
450 ligand binding energies (**Supp Table 7**). ΔG_{bind} calculations performed both with and without phospholipids
451 indicated that the presence of POPC-A and POPC-B generally leads to more thermodynamically favorable
452 ΔG_{bind} energy values for most of the compounds tested.

453 Among the compounds, FM1-43[57–59] (**Figure 4D** and **Figure 5A**) and E6-berbamine[54], which have distinct
454 structural scaffolds yet fitting similar pharmacophores (**Figure 1, Figure 3, Table 1**, and **Supp Table 2**)
455 exhibited the strongest binding affinities with and without phospholipids (**Supp Table 1** and **Supp Table**
456 **7**), consistent with their reported channel blocking potencies[54,57–59]. While hexamethyleneamiloride
457 showed a slightly higher ΔG_{bind} value, UoS-7692 displayed a less negative ΔG_{bind} value, possibly due to
458 the presence of the two fluorine substituents in acetophenone moiety at *meta* and *para* positions. Overall,
459 our molecular docking and MM-GBSA analyses suggest that phospholipids may enhance the strength of
460 TMC1-blocker interactions.

461 ***Binding modes and affinities of newly identified hit compounds within the TMC1 pore.***

462 We next implemented the same *in silico* strategy to the compounds obtained from PBVS in the two
463 libraries:

464 *Library 1 (non-FDA-approved compounds):* Our initial analysis focused on the best 200 compounds from
465 Library 1 with the lowest MM-GBSA ΔG_{bind} values, without considering phospholipids. However, only 45
466 of these compounds were commercially available for subsequent *in silico* experiments (**Supp Table 8**).
467 Using the Tanimoto-similarity coefficient[123] (see *Methods*) we identified structurally diverse compounds,
468 resulting in 15 different molecular clusters (See cluster IDs in **Supp Table 8**). From these, we selected hit
469 compounds based on binding affinities from clusters that included 3 or more compounds. Specifically,
470 three hits with the lowest ΔG_{bind} values (without phospholipids) were selected as representatives from
471 clusters 1.1 and 1.2, while one hit was selected to represent clusters 1.3 to 1.6 (**Supp Table 8**).

472 *Library 2 (FDA-approved drugs):* Among the 53 compounds analyzed from Library 2, all of which were
473 commercially available, the Tanimoto-structural diversity analysis provided 10 different molecular clusters
474 (see cluster IDs in **Supp Table 8**). One compound with the lowest ΔG_{bind} value (MM-GBSA without
475 phospholipids) was selected from each cluster for further evaluation.

476 We subsequently verified whether the selected hits identified through MM-GBSA and Tanimoto analysis
477 without phospholipids also exhibited thermodynamically favorable MM-GBSA ΔG_{bind} energies in the
478 presence of phospholipids. As with the known blockers (**Supp Table 7**), MM-GBSA results in the presence

479 of phospholipids generally showed improved ΔG_{bind} energies for hit compounds from both libraries. This
480 confirmed that the selected hits after MM-GBSA and Tanimoto analysis were consistently top ranked in
481 both MM-GBSA subgroups, with and without phospholipids (**Table 2**). Ultimately, 10 hits were selected
482 from each library for experimental evaluation in cultured cochlear explants (**Table 2, Figures 7-8**).

483 Next, we analyzed the binding interactions for selected newly identified compounds within the TMC1 pore,
484 focusing on their binding within the top, middle, and bottom sites of the pore, as guided by HOLE analysis
485 and molecular docking (**Figure 2B** and **Figure 5**). Below, we describe interactions for some representative
486 molecules.

487 Posaconazole is predicted to establish key contacts within the TMC1 pore (**Figure 5D**). Its molecular
488 length, measured using *Maestro* software package, suggested an extensive length of 28 Å (end-to-end
489 distance), allowing posaconazole to interact across the pore. At the top site, the triazole ring forms a
490 hydrogen bond with N404 and polar interactions with the phosphate head of POPC-B at the ZN1 site. In
491 the middle region, the dichlorophenyl-furan moiety of posaconazole stacks against M403, M407, and
492 F451. The aromatic rings display van der Waals interactions with residues on TM5, TM6, and TM7 where
493 the positively charged piperazine ring forms a salt bridge with D528 (3.02 Å) in the ZN2 site. At the bottom
494 site of the pore, the triazinone ring forms a hydrogen bond with N573 and the hydroxyl group interacts with
495 D540 in the ZN3 pocket.

496 Another non-FDA-approved compound, ZINC24739924, docked at the bottom site of the pore, forming
497 close contacts with residues of TM8 (**Figure 5E**). The benzotriazinone moiety of ZINC24739924 stacks in
498 the ZN3 pocket between the polar head of POPC-A, T535, D540, and N573. The charged triazine group
499 makes close contacts with D540, F568, and N573. In addition, the positively charged amine forms a
500 hydrogen bond with the phosphate group of POPC-B, while the benzyl moiety forms van der Waals
501 contacts with M412 and the tails of both POPC-A and POPC-B, stabilizing the ligand (**Figures 5E** and **5I**).
502 Furthermore, the trifluoro-methoxy substituent exhibits polar interactions with T535 (3.16 Å) of the ZN3
503 site. A similar binding pattern was observed for another novel TMC1 modulator, ZINC58438263, which
504 has a 3-methyl-anisole moiety and binds to the ZN3 site of TMC1 (**Supp Figure 5**).

505 Finally, the FDA-approved drug cepharanthine shared similar interactions to its homolog alkaloid
506 tubocurarine within the top, middle, and bottom sites of the TMC1 pore (**Figure 5F**). Similar to FM1-43,
507 molecular docking and HOLE showed that its positively charged nitrogen is located within the predicted
508 pore radius of TMC1 (**Supp Figure 6**). At the top site, the methoxybenzene moiety displays hydrophobic
509 interactions with N404 and polar interactions with S408 (3.98 Å) on TM4. In the middle site, the aromatic
510 rings stacked towards the TM4, TM5, and TM7 domains, positioning the methylated methoxy-
511 dihydroisoquinoline and the dioxolane moieties between the TM5 and TM7 helices near residues L444
512 (TM5) and F579 (TM7). The second protonated dihydroisoquinoline is positioned towards the TM4 helix
513 close to M412 (3.44 Å), G411 (3.73 Å), and the hydrophobic tail of POPC-B (3.49 Å). Unlike tubocurarine,
514 cepharanthine did not form a direct interaction between its protonated amine and D569 or the polar head
515 of POPC-A. However, it is possible that water molecules could facilitate these interactions at the
516 cytoplasmic region of the ZN3 pocket (**Figure 5F**).

517 ***Identification of key residues modulating TMC1-ligand interactions***

518 We conducted a comprehensive structural analysis of residues within a 5 Å radius of each docked
519 compound within the pore cavity to identify key TMC1-ligand interactions. This analysis included 16 known
520 MET channel blockers, and 20 hit compounds from *Libraries* 1 and 2 (**Supp Table 7**, **Table 2**, **Figure 7**),
521 totaling 36 compounds. We examined all TMC1 residues lining the pore based on their contact frequency
522 with the ligands, as determined by our docking and MM-GBSA pipeline analysis. Residues were
523 categorized as high-contact (contact frequency >0.5) or low- contact (contact frequency <0.5), indicating
524 whether more than 50% or less than 50% of evaluated ligands interacted with each residue, respectively
525 (**Supp Figure 7**, with residues scoring above or below the *red dashed line*).

526 Notably, several previously characterized residues known to influence TMC1 channel function, such as
527 *Mm*TMC1 M412, D528, T531, and D569[18,90,115,119,124–127], were identified as high-contact-frequency

residues in this study, suggesting their accessibility for ligand interactions. More importantly, we also identified a set of novel residues with contact frequencies exceeding 0.5, indicating their likely involvement in modulating TMC1-ligand interactions. These residues include M407, S408, G411, P415, T416, I440, L444, N447, L524, T532, T535, G572, N573, A576, F579, M583, and R601.

Additionally, both POPC phospholipids showed the highest contacts frequencies, suggesting that they may play a significant role in modulating TMC1 function. In summary, our pipeline, which combines molecular docking with MM-GBSA, effectively predicts high-contact-frequency residues that are likely to modulate TMC1-ligand binding across the three druggable binding sites along the TMC1 pore.

Validation of novel TMC1 modulators in cochlear hair cells using AM1-43 dye loading assay.

To validate our *in silico* findings, we conducted a fluorescent dye loading assay using the FM1-43 analogue, AM1-43, to assess the ability of newly identified compounds to block the MET channel in murine cochlear hair cells. When briefly introduced into the bath solution, these large, positively charged fluorescent dyes enter hair cells through MET channels, which are open at rest. As such, FM1-43 and AM1-43 are commonly used as indicators of MET channel activity, allowing us to evaluate the effectiveness of each compound in interacting with the pore and modulating the dye loading through the MET channel (**Figure 8**).

For these experiments, cochlear explants from postnatal day 3 (P3) mice were cultured for two days *in vitro* at 37 °C and 8% CO_2. The explants were then exposed to either AM1-43 alone (positive control, supplemented with 2% DMSO) or in combination with the compound for 60 seconds, following a prior 60-second pre-incubation with the compound. After rinsing off excess dye and neutralizing background fluorescence with the 4-sulfonate calix[8]arene sodium salt (SCAS) quencher, live imaging of the explants was conducted using confocal microscopy.

The fluorescence intensity levels of outer hair cells were individually quantified using the *Cellpose* algorithm[128] and normalized to the average values measured from explants treated with AM1-43 only, separately for each experimental session. As an additional control, we incubated some cochlear explants with 100 µM tubocurarine or benzamil, two well-established potent MET channel blockers known to largely prevent FM1-43 uptake[19,112,114] (see *Methods*). All compounds tested *in vitro* were applied at a standardized concentration of 100 µM (**Figure 8**).

Of the 20 structurally diverse hit compounds (**Table 2**), representing 10 compounds from each library, only 15 were tested *ex vivo* due to commercial availability. Most compounds (7 out of 15) showed a significant reduction in the AM1-43 dye loading through the MET channel (**Figure 8** and **Supp Figure 8**). We used an arbitrary 60% cut-off threshold as indicative of an effective blockage, with the control values representing 100% fluorescence levels (**Supp Figure 8**).

From *Library 1,* the compounds ZINC24739924 (56.25 ± 21.29%), ZINC12986242 (46.1 ± 14.28%), ZINC12430014 (60.94 ± 15.64), ZINC58438263 (46.8 ± 18.59%), showed significant reductions of AM1-43 uptake. From *Library 2*, posaconazole (60.02 ± 19.12%), pyrithioxine (also called pyrithioxin or pyritinol) (53.52 ± 30.18%), and cepharanthine (48.09 ± 20.72%) exhibited the most promising results. Despite being less effective, ZINC06530230, nefazodone, indinavir, lapatinib, and ceforanide still significantly reduced AM1-43 loading. Interestingly, amitraz from *Library 2* appeared to have the opposite effect, increasing AM1-43 loading into OHCs (122.4 ± 21.64%; **Supp Figure 8**).

We selected representative compounds that interact within the top, middle, and bottom sites of the TMC1 pore for illustration (**Figure 5**): posaconazole, cepharanthine, and ZINC24739924, three effective blockers that reduced hair cell MET-mediated AM1-43 dye loading by approximately 50% (**Figure 8**, and **Supp Figure 8**). Overall, our *ex vivo* results align with our *in silico* predictions, indicating that compounds that were predicted to be thermodynamically favorable to interact within the TMC1 pore showed moderate but significant reductions of AM1-43 loading when tested in cochlear hair cells. Further *in vitro* evaluation with additional biological replicates and single-cell electrophysiology is needed to carefully assess the potency of each hit compound. Thus, this ex *vivo* results support the efficacy of our *in silico* pipeline in identifying

576 novel MET channel modulators within a chemical space of millions of compounds and understanding their
577 potential binding interactions within the TMC1 pore.

578 ***Cepharanthine's dual role in TMC1 and TMEM16A modulation suggests shared pharmacophores.***

579 Because of the structural and evolutionary relationship between the TMC and TMEM16 families of
580 proteins[18,62,63,129], the structure and electrophysiological properties of TMEM16 proteins have garnered
581 significant interest in studies involving TMCs. Interestingly, cepharanthine, one of the most potent FDA-
582 approved drugs identified in this study for reducing the AM1-43 loading into cochlear hair cells (**Figure 8**),
583 has also been previously reported to inhibit TMEM16A[87,130]. Therefore, we investigated whether inhibitors
584 of both TMC1 and TMEM16A proteins share common pharmacophoric features.

585 To do this, we used *Phase* to virtually screen 10 known modulators of TMEM16A (MONNA, Ani9, TMinh-
586 23, Zafirlukast, Niclosamide, Evodiamine, Tannic acid, theaflavin, E_{act}, and F_{act})[87,130] against the 10 TMC1
587 pharmacophores (**Table 1**, and **Supp Figure 3**). Our results indicate that both cepharanthine and
588 theaflavin share the same APRR pharmacophore (theaflavin matches with 9 pharmacophores). Although
589 theaflavin lacks a protonatable amine, *Epik* predicted a protonated carbonyl group instead (**Supp Figures**
590 **9A-D**). Additionally, the ARR-2 pharmacophore exhibited similar vector features between cepharanthine
591 and Ani9, a known inhibitor of TMEM16A (Ani9 matches with 6 pharmacophores) (**Supp Figures 9E-H**).

592 Our predicted docking poses for cepharanthine indicate that it binds primarily at the middle and bottom
593 sites of the *Mm*TMC1 pore, with some interactions at the top site near N404 (**Figure 5F**, **6E-H**, and **Supp**
594 **Figures 9E-G**). However, previous studies have predicted and tested cepharanthine and theaflavin
595 binding to TMEM16A specifically towards the top site of the pore[87,130].

596 To better understand these discrepancies, we performed a comparative structural analysis between our
597 open-like state of the *Mm*TMC1 model and the reported *Mm*TMEM16 structure (PDB code: 5OYB)[131]
598 (**Supp Figures 9I-L**). As reported in the literature, the *Mm*TMEM16 structure was used to predict the
599 binding mode of cepharanthine and theaflavin only at the top site of the pore region[87,130], equivalent to the
600 top site within the TMC1 pore (**Supp Figures 9I-L**). Preciously reported docking-guided site-directed
601 mutagenesis experiments and *in silico* MD simulations have shown that mutations at the upper binding
602 pocket of *Mm*TMEM16A attenuate the ability of cepharanthine and theaflavin to inhibit *Mm*TMEM16A
603 currents[87,132].

604 The predicted *Mm*TMEM16A upper-binding pocket and the reported mutations can explain the decreased
605 affinity of cepharathine and theaflavin if they only bind at the extracellular pocket of TMEM16A[132].
606 However, it is possible that open conformations of the *Mm*TMEM16 pore might expose druggable sites at
607 the middle and bottom areas of the pore, as we predicted for TMC1 in this study (**Figures 4-5**, and **Supp**
608 **Figure 5**).

609 However, it is possible that the predicted docking poses for *Mm*TMEM16A at its upper pocket site may
610 have been influenced by a closed conformation of *Mm*TMEM16A and/or restricted by the use of smaller
611 gridboxes[87,132] during docking sampling. Consequently, the conformational space explored in
612 *Mm*TMEM16A might not have sampled potential druggable sites of cepharanthine and theaflavin within
613 the middle and bottom sites of the pore[87,132], as predicted for TMC1 in our study. This is consistent with
614 recent reports of open conformations of *Mm*TMEM16A and newly identified druggable pocket binding sites
615 across the pore[133,134].

616 **DISCUSSION**

617 TMC1 is a nonselective cation channel which primarily mediates the influx of Ca^{2+} and K^{+} into hair cells in
618 response to mechanical stimulation. Unlike other cation channels, TMC1 lacks a conventional cylindrical
619 pore selectivity filter[82], instead featuring a long-curved pore cavity that may be partially exposed to the
620 plasma membrane[21,55,90]. This structure allows TMC1 to be significantly permeable to bulky organic
621 molecules, such as FM1-43[57,58], AGs[17] and other large compounds. In fact, compounds as large as 3 kDa

622 dextrans have been shown to permeate through TMC1[135]. However, the atomic-level interactions of these
623 compounds within the MET channel pore remains poorly understood.

624 TMC1's permeability to aminoglycosides underscores its relevance in the context of aminoglycoside-
625 induced ototoxicity, a major concern in hearing health. Advancing our understanding of how these
626 compounds interact within the TMC1 pore could lead to the identification of novel otoprotective solutions
627 to mitigate AG-induced hair cell damage.

628 The main objective of this study was to identify the common structural features of known MET blockers
629 and use this information to develop a pipeline for discovering novel MET modulators. Additionally, we
630 aimed to explore how these modulators might interact within the TMC1 pore. To achieve this, we employed
631 a comprehensive *in silico* approach that included 3D-pharmacophore modeling, *AlphaFold2* modelling,
632 molecular docking, Tanimoto similarity analysis, and MM-GBSA ΔG_{bind} analysis. We screened two
633 compound libraries and identified 10 novel non-FDA-approved compounds and 10 FDA-approved drugs
634 as candidates from a pool of over 230 million compounds. Seven of the 15 experimentally tested
635 compounds showed a significant reduction in AM1-43 dye loading into hair cells (**Figure 8** and **Supp**
636 **Figure 8**), validating our approach.

637 Our *in silico* findings demonstrate that TMC1 possesses an enlarged cavity with druggable ligand-binding
638 sites, capable of accommodating small molecules[55,136]. We estimate that the pore's narrowest dimension
639 is approximately 4.5 Å diameter, which is larger than previously reported pore sizes (**Figure 2B**). This
640 enlarged cavity provides multiple binding sites in the top, middle, and bottom regions of the TMC1 pore,
641 which can accommodate a variety of ligands.

642 A key outcome of this study is the development of universal 3D-pharmacophore models for MET blockers.
643 These models can be used to screen millions of compounds *in silico* for further *in vitro* testing in hair cells.
644 To our knowledge, this is the first *in silico* pipeline that combines molecular pharmacophore modeling, MD
645 simulations, docking, and MM-GBSA analysis to identify novel MET channel modulators. Furthermore,
646 this study also identified novel atomic details of ligand interactions within the TMC1 pore, revealing a
647 synergistic combination of amino acids that form distinct druggable-binding sites at the top, middle, and
648 bottom sites of the TMC1 pore cavity.

649 Based on the docking poses of FM1-43 and AM1-43 (**Figure 5A**, and **Supp Figure 5**), we infer that the
650 tight packing of both the triethylammonium and the dibutylamine groups at the top binding site of the TMC1
651 pore, along with the presence phospholipids molecules, may explain why bulkier molecules such as FM3-
652 25 fail to block MET currents[58]. Additionally, this tight packing could contribute to the slower permeation
653 of these bulkier molecules compared to the fast uptake of FM1-43 in hair cells[59].

654 The results presented in this work strongly support the idea that the ligands bind to key residues within
655 the TMC1 pore, including M412, D528, T531, and D569. These residues have been shown influence both
656 the blocking effects of certain compounds (e.g., DHS, FM1-43) and the ion permeability of
657 TMC1[18,90,115,119,124–127]. Mutations in residues such as D528, D569, and M412 are known to cause deafness
658 and alter mechanotransduction current properties of TMC1[85,118,137]. This indicates that residues involved
659 in modulation of the ion conductance may also play a role in TMC1-ligand interactions. However, our
660 docking predictions suggest that the pathways for ion-conduction and ligand-permeation within the TMC1
661 pore might be distinct, as chemical moieties of several docked ligands were predicted to bind in regions
662 outside the predicted pore contour identified by HOLE analysis (**Supp Figure 6**).

663 Our docking results accurately predicted several residues that interact with known MET blockers, which
664 have been well-experimentally characterized in mice through point mutations in TMC1[18,90,115,119,124–127].
665 These mutations have demonstrated the importance of these residues in permeation and block. Future
666 studies involving site-direct mutagenesis and single-cell electrophysiology will allow to evaluate and further
667 validate the novel contact residues identified in this study.

668 Our MD simulations, docking predictions, and MM-GBSA energy analyses suggest that phospholipids play
669 a key role in small molecule binding, mediating hydrogen bonds, salt bridges, and hydrophobic interactions
670 within the TMC1 pore (**Figure 4C,** and **4G-I, Figure 5G-I**). These findings suggest that proper membrane

671 function around TMC1 promotes stable ligand binding. This in agreement with experimental observations
672 showing that blockage of TMC1 with high concentrations of benzamil and tubocurarine triggers membrane
673 scrambling and phosphatidylserine externalization in hair-cell stereocilia bundles[114]. Compared to
674 previous simulations of TMC1 and TMC1+CIB2, which did not include TMIE as part of the MET complex,
675 our results reveal possible functional implications of the "elbow-like" linker of TMIE as a flexible component
676 of the mammalian MET channel. Notably, flexibility has also been reported for the PCDH15 MAD12
677 domain, another part of the MET complex, which has been shown to exhibit mechanical weakness under
678 force stimulation[138]. Furthermore, while our results suggest that the C-terminal helix segment of TMIE
679 exhibits flexibility, this observation may complement experimental data indicating its role as a target region
680 for phosphatidylinositol 4,5-bisphosphate (PIP_2) binding. This region has been implicated in regulating
681 MET currents, and potentially coupling TMIE with PIP_2 to the plasma membrane[139]. However, further
682 studies are necessary to directly determine how flexibility might influence its interaction with PIP2 and its
683 functional implications in the MET complex.

684 Additionally, the docking and MM-GBSA data show M412 in close contact with phospholipids, also
685 reported as one of high-frequency ligand-binding residues. This may help explain why charged mutations
686 like M412K increase annexin V (AnV) signals, as the p.M412K mutation might attract the phospholipid
687 heads, promoting membrane scrambling[114]. Our docking interactions of both benzamil and tubocurarine
688 further support the hypothesis that phospholipids act as ligand-binding modulators (**Figure 4-6, Supp**
689 **Figure 5**, and **Table 2**).

690 Since the hit compounds were evaluated in early postnatal cochlear explants (P3+2 days *in vitro*), their
691 blocking potency might have been influenced by the overwhelming presence of TMC2 during that
692 developmental stage in the mouse cochlea, which was not considered in our *in silico* predictions. TMC2
693 is transiently expressed in mouse cochlear hair cells during early development and at the onset of the
694 hair-cell mechanotransduction, but is gradually downregulated and is replaced by TMC1 around P10[140,141].
695 Therefore, selective screening and design of TMC1 blockers may necessitate experimental evaluation in
696 mature cochlear hair cells in the absence of TMC2, or in *Tmc2*-ko mice. However, because the screened
697 compounds were based on pharmacophore models of known MET blockers, they likely display some
698 blocking capability for both TMC1 and TMC2. This hypothesis could be further validated using *Tmc1*-ko
699 and/or *Tmc2-ko* mice[142].

700 However, the structural exclusion of TMC2 from our *in silico* pipeline may promote the selection of hit
701 candidates with possible increased selectivity for TMC1, since the putative pore of TMC2 is distinct from
702 TMC1[143]. The TMC2 pore displays decreased hydrophobicity and a smaller pore radius compared to the
703 homologous middle site of TMC1. These characteristics may reduce the affinity of TMC2-ligand
704 interactions[143]. It is well known that most small molecules preferentially bind to hydrophobic pockets[144],
705 highlighting the complexity of TMC1-blocker interactions within the druggable-pore cavity and the high
706 variety of amino acids involved in TMC1-ligand binding. This structural complexity suggests that the
707 binding affinities of compounds with MET-blocker properties may vary depending on TMC isoform and,
708 perhaps, even species.

709 TMCs belong to a larger superfamily that includes TMEM16 and TMEM63/OSCA proteins[62]. Our study not
710 only sheds light on the structural features required to modulate the uptake capacity of TMC1 proteins but
711 also provides key insights on potential pharmacological relationships between TMC1 and TMEM16A
712 proteins, as they share common 3D pharmacophores for their compound antagonists. In addition, this
713 study provides additional structural and functional insights into the role of the TMC1 pore in hair cells[145].

714 In summary, our combined *in silico* and *in vitro* experimental study suggest that a pharmacophore
715 composed by two aromatic groups, one acceptor group, and at least one protonatable amine is required
716 for blocking the TMC1 pore cavity of the mammalian hair-cell MET channel. We developed and provided
717 a proof-of-concept validation of a pipeline for discovering novel MET channel modulators. Our pipeline
718 successfully identified compound antagonists of the hair-cell MET function able to reduce AM1-43 loading
719 into cochlear hair cells *in vitro*. Further evaluation of the reported compounds will provide more insights
720 into their modulatory capacities and help identify novel MET blockers, study their potential otoprotective

721 applications, as well as their plausible role in TMEM16A modulation. Additionally, future studies using site-
722 directed mutagenesis will help elucidate the role of high-contact druggable sites in TMC1-ligand binding,
723 their impact on hair-cell mechanotransduction function, and their potential influence on TMC1 ion
724 selectivity and conductance.

725 MATERIALS AND METHODS

726 *AlphaFold2 modeling of the MET complex structure*

727 We generated a dimeric structural model of *Mm*TMC1, spanning residues 81-746, adopting an open-like
728 conformation[85] with domain swapping feature at transmembrane domain 10 (TM10). This model was
729 constructed using *AlphaFold2* through the ColabFold GitHub repository[146]. Subsequently, the MET
730 complex was constructed, also using *AlphaFold2*, by combining two TMC1 subunits, each accompanied
731 with CIB2 (residues 1-187) and TMIE (residues 44-118) in a 1:1:1 ratio[55,147,148].

732 The resulting MET complex model was then compared with the structure of the expanded *C. elegans*
733 TMC-1 complex (PDB code: 7USW)[55], showing the typical swapped conformation and location of homolog
734 binding partners of the MET complex.

735 *Molecular dynamics simulations*

736 The modeled MET complex was prepared using the protein preparation wizard module of the *Maestro*
737 suite[110,111,149]. Amino acid protonation states were assigned at pH 7.4 using PROPKA[150]. Subsequently,
738 the complex was subjected to energy minimization and embedded into a pre-equilibrated POPC bilayer,
739 followed by solvation using the SPC water model. To neutralize the system, ten K^+ ions were added, and
740 the final ion concentration was set to 0.15 M KCl. Molecular dynamics simulations were performed with
741 *Desmond*[151] and the OPLS4 force field[152].

742 The *Desmond* default membrane relaxation protocol was applied before simulations. Then, 25 ns of
743 equilibrium MDs in a NPγT semi-isotropic assembly were performed, applying restrictions to the protein
744 backbone (spring constant 10 kcal × mol^{-1} × $Å^{-2}$) with constant surface tension of 0.0 bar × Å. Temperature
745 and pressure were kept constant at 300 K and 1.01325 bar, respectively, by coupling to a Nose-Hoover
746 Chain thermostat[153] and Martyna-Tobias-Klein barostat[154] with an integration time step of 2 fs. Coulombic
747 interactions were calculated using a cutoff of 9 Å. Subsequently, three replicates of 25 ns production MDs
748 were performed using the last frame. Restrictions were applied to the protein secondary structure (spring
749 constant 5 kcal × mol x A^2) under the same conditions as described above. Replicates' statistical analysis
750 is available at the Ramirez Lab Github repository (see *Data availability section*). We also extended the
751 production 25 ns MD to 100 ns to study the stability of the MET complex. The production 25 ns and 100
752 ns MDs were analyzed with *Desmond* and in-house scripts. Visualization was carried out with VMD[155] and
753 Pymol[156]. Subsequently, we analyzed the pore with the HOLE algorithm. Pore radius measurements of
754 the TMC1 chain A were obtained over 25 ns and 100 ns production trajectories to determine the stability
755 of the pore and the TMC1 dimer. Measurements were obtained every nanosecond throughout the
756 simulations. The 25 ns MDs equilibrated structure was used for further virtual screening. In addition, we
757 analyzed the potential location of phospholipids neighboring the TMC1 pore.

758 *Ligand-based pharmacophore modeling of known MET blockers*

759 Thirteen MET channel blockers with structural diversity reported in the literature such us UoS-7692[33],
760 UoS-3607[33], UoS-3606[33], UoS-5247[33], UoS-962[33], Proto-1[98], E6-berbamine[54], hexamethyleneamiloride[37],
761 amsacrine[37], phenoxybenzamine[37,99], carvedilol-derivate 13[53], ORC-13661[34,36], and FM1-43 (a positively
762 charged styryl dye often used to label hair cells)[58,59], were selected to design 3D-pharmacophore models
763 of small molecules using an energy-optimized pharmacophore method.

764 The pharmacophore design is a versatile approach used to extract common chemical features from a set
765 of small molecules with biological function. First, the structures of the 13 known MET channel blockers
766 were sketched using *Maestro*[91] and then prepared using *LigPrep*[109] (Schrödinger, 2021) with the S-OPLS
767 force.

768 Salts were removed and no tautomers were generated, compound chiralities were determined from the
769 reference 3D structure. Subsequently, both pharmacophore and ligand mapping were generated from the
770 13 MET blockers selected, with the *Phase* module[68]. We used six pharmacophoric features: Hydrogen
771 bond acceptor (A), hydrogen bond donor (D), hydrophobic group (H), negatively charged group (N),
772 positively charged group (P), and aromatic ring (R).

773 To model the pharmacophores, a minimum of 3 and maximum of 5 pharmacophoric features were set.
774 Also, the percentage of pharmacophore matching threshold (number of known blockers that fits to the
775 modeled pharmacophore) of 50% was selected as a minimal criterion for a representative pharmacophore
776 model of the 13 known MET blockers. The other settings in *Phase* were used by default. Finally, the best
777 10 pharmacophore models were ranked using the *PhaseHypoScore*[68]. This score measures how well the
778 pharmacophoric-feature vectors align with the structures of the compounds that contribute to the 3D-
779 pharmacophore model.

780 To validate our pharmacophore models, we use active compounds (known MET channel blockers) and
781 decoys (40 decoys per active) generated with *LIDeB*[157] (**Supp Table 3**). To evaluate the performance of
782 each pharmacophore, different key measures were considered, including the area under the curve (AUC)
783 of the corresponding receiver operating characteristic (ROC) as described[158]. In addition, we calculated
784 the percentage of actives (% Yield), the percentage yield of active compounds (Ya), sensitivity (Se),
785 specificity (Sp), enrichment factor (EF), and the Güner-Henry (GH) scoring using the method reported in
786 the literature[102].

787 *Pharmacophore based virtual screening (PBVS)*

788 In this project, we used two molecule libraries. *Library* 1 (non-FDA-approved compounds) from the ZINC
789 database (ZINC20) contains over 230 million commercially available compounds in 3D formats and over
790 750 million purchasable analogs[105]. *Library* 2 (1,789 FDA-approved drugs — US Drug Collection,
791 MicroSource Discovery Systems)[106] was in-house processed for PBVS using the *LigPrep* and *Epik*
792 modules of *Maestro*[91,109,110] with the OPLS3 force field[159]. All possible ionization states were predicted for
793 each compound at pH 7.4 ± 2.0, and their chiralities were retained.

794 We carried out a two-step PBVS with the non-FDA-approved *Library* 1. The 1st-step PBVS using the
795 software *ZINCPharmer*[107], followed by a 2nd-step screening with *Phase*. For the *ZINCPharmer* screening,
796 the 10 best pharmacophores generated after the pharmacophore mapping step were used to search the
797 most promising compounds from ZINC20 that fits with any of the 10 pharmacophore models.

798 Compounds were filtered by selecting a single hit as the maximum limit per conformation for each molecule
799 having a maximum RMSD geometric match of 1 Å against each of the 10 pharmacophore models
800 (compounds with RMSD > 1 Å were discarded). The best 50,000 hits (5,000 per each pharmacophore
801 model) with molecular weights between 200 and 700 g/mol were selected from ZINC20. Finally, we
802 selected the compounds that matched two or more pharmacophores using the *KNIME* software[160].

803 For the 2nd-step PBVS, the compounds from the 1st-step (*Library* 1) were processed with *LigPrep*, and
804 ionization states were generated at pH 7.4 ± 0.5 using *Epik*[110,111]. In parallel, the *Library* 2 (FDA-approved
805 drugs) were also processed with *LigPrep* and *Epik*. Thus, the prepared molecules from both libraries were
806 screened against each of the 10 pharmacophores using *Phase*, following the methodology reported by
807 Gallego-Yerga et al., 2021[153].

808 For both libraries, the *PhaseScreenScore* values (which evaluate how well the ligands align to the
809 pharmacophore features of the hypothesis)[161] were obtained for each ligand per screening against each
810 pharmacophore. In addition, we implemented a workflow with *KNIME* analytics platform and built a matrix
811 to calculate the *Total-PhaseScreenScore* (TPS_S) for each ligand, represented by the sum of each
812 *PhaseScreenScore* value. Then, we selected hits for molecular docking if the value was higher than the
813 docking threshold (D_T) value, according to the equation 1.
814
815 $$D_T \geq \bar{X} + 2\delta \quad \text{(Eq. 1).}$$
816

817 D_T is the docking threshold, $\bar{X}$ is the average TPS_S of the entire *Library* (1 or 2) solutions; and δ is the
818 TPS_S standard deviation of the entire *Library* (1 or 2) solutions.

819 *Molecular docking and free energy binding energy calculations*

820 After PBVS, molecules from both libraries were docked with the *Glide* software[117] in the pore of the
821 *Mm*TMC1 model (in complex with CIB2 and TMIE) using the frame structure at 24 ns post-equilibration.
822 The protein complex and all the phospholipids were kept for molecular docking, while waters and ions
823 were removed. A cubic gridbox of ($41_x \times 41_y \times 41_z$) $Å^3$ was centered at methionine M412 (chain A) covering
824 the TMC1 pore including part of the TMIE helical protein embedded in the membrane (**Figure 2**).

825 Molecular docking was performed for the selected hits with the best *PhaseScreenScore* criteria from
826 libraries 1 and 2, overpassing the docking threshold, as well as for the 13 known MET blockers (UoS-
827 7692, UoS-3607, UoS-3606, UoS-5247, UoS-962, Proto-1, E6-berbamine, hexamethyleneamiloride,
828 amsacrine, phenoxybenzamine, carvedilol-derivate 13, ORC-13661 and FM1-43), benzamil, tubocurarine,
829 and DHS (known experimental molecules used as MET channel blockers) (**Figure 1**, **Figure 4**, and **Figure**
830 **6**). The Glide standard precision (SP) mode and the OPLS_2005 force field were used to explore the
831 positional, conformational, and orientational space of the ligands in the TMC1 pore.

832 A maximum of 10 docking poses were requested for each ligand and the best pose was determined by
833 selecting the conformer with the lowest *Glide Emodel* score followed by a low *Glide Score* value from
834 superposed-like poses[117]. The *Glide Emodel* was prioritized, since *Glide* uses *Emodel* to pick the best
835 pose of a ligand (conformer selection) and subsequently rank them against one another using
836 *GlideScore*[117]. A manual check of each representative pose was carried out to identify common binding
837 sites for each selected pose from each molecular docking cluster.

838 Molecular docking solutions from both libraries 1 and 2 were rescored by calculating their binding free
839 energies (ΔG_{Bind}). Two docking postprocessing strategies were implemented. **Strategy A**: excluding
840 phospholipids neighboring the pore, and **strategy B**: including key phospholipids neighboring the pore
841 that could influence small molecule binding. ΔG_{Bind} calculations were carried out using MM-GBSA
842 methods[86] with *Prime*[162], combining molecular mechanics energies and implicit solvation models[163]. The
843 MM-GBSA ΔG_{Bind} between ligands and the TMC1 channel was calculated with the following equations:

844

845 $$\Delta G_{bind} = \Delta H - T\Delta S \approx \Delta E_{MM} + \Delta G_{sol} - T\Delta S, \quad \text{(Eq. 2)}$$
846 $$\Delta E_{MM} = \Delta E_{internal} + \Delta E_{electrostatic} + \Delta E_{vdw};\ \Delta G_{sol} = \Delta G_{PB/GB} + \Delta G_{SA}, \quad \text{(Eq. 3)}$$

847

848 where ΔE_{MM}, ΔG_{sol}, and $-T\Delta S$ are the changes in the molecular mechanics energy, solvation-free energy,
849 and conformational entropy upon binding, respectively. ΔE_{MM} includes $\Delta E_{internal}$ (bond, angle, and dihedral
850 energies), electrostatic, and van der Waals energies. ΔG_{sol} is the sum of the electrostatic solvation energy,
851 $\Delta G_{PB/GB}$ (polar contribution), and non-electrostatic solvation, ΔG_{SA} (non-polar contribution). The polar
852 contribution was calculated by using the generalized born model, while the non-polar energy was
853 calculated by the solvent accessible surface area (SASA). The VSGB 2.0[164] solvation model and OPLS
854 force field were used for these calculations. Residues located within 5 Å from the ligands were included in
855 the flexible region, and the rest of the protein atoms were kept frozen.

856 *Morgan fingerprint and Tanimoto-similarity coefficient*

857 After virtual screening through both libraries, Morgan fingerprint similarity factors[165] were determined for
858 all molecules with the *RDKit* module of the *KNIME* analytics platform. This extended-connectivity
859 fingerprint based on Morgan algorithm represent molecules as mathematical objects, which allow us to
860 analyze the structural environment of each atom up to a radius of 2 Å[165]. Using the Morgan fingerprint, we
861 calculated the distance matrix with the Tanimoto-similarity coefficient[123], which allowed us to determine
862 the structural similarity of the compounds on a scale from 0 (non-identical) to 1 (identical).

863 Then hierarchical clustering was performed with the average linkage method. Clusters were selected using
864 the normalized distance threshold of 0.75 for the non-FDA-approved dataset (*Library* 1) and 0.85 for the

FDA-approved dataset (*Library* 2) to enhance structural diversity. Representative compounds for populated clusters were selected for further evaluation.

Mouse cochlear explant cultures

All procedures and protocols were approved by the Institutional Animal Care and Use Committee of Mass Eye and Ear and we have complied with all relevant ethical regulations for animal use. Postnatal day (P) 3 CD-1 mice of either sex were cryo-anesthetized and euthanized by decapitation. Inner ears were harvested and organ of Corti epithelia were acutely dissected in Leibovitz's L-15 (L-15, Gibco #21083027) cell culture medium. Following dissection, explants were affixed to glass-bottom cell culture dishes coated with Geltrex basement membrane matrix (Gibco #A1569601, 100 μL/dish) and cultured in DMEM (Gibco #12430054) supplemented with 3% FBS and 10 mg/L ampicillin for 48 hours at 37 °C, 8% CO_2.

Dye loading and fluorescence imaging

Cochlear explants from postnatal day 3 (P3) mice were cultured for two days *in vitro* at 37 °C and 8% CO_2. Following gentle aspiration of the culture medium at room temperature, the explants were rinsed with L-15 and were pre-treated for 60 s with the compound at a final concentration of 100 μM (dissolved in L-15 at 2% DMSO). The solution was then aspirated and replaced with a solution consisting of the loading dye AM1-43 (4 μM) and the hit compound (100 μM) of in L-15 with 2% DMSO). Following another 60 s of incubation, the solution was aspirated, and the excess AM1-43 dye was neutralized using a quenching solution composed of 0.2 mM 4-sulfonate calix[8]arene sodium salt (SCAS, Biotium) in L-15.

Live imaging of the samples was performed using a Leica SP5 confocal microscope equipped with a 40×, 0.8 NA water-dipping objective lens, zoom was set to 2×, resulting in an effective pixel size 189nm. The laser power and smart gain settings were kept constant across all experimental conditions. During each experimental session, at least one compound and one control sample were imaged.

Image analysis

Following image acquisition, maximum intensity z-projections were generated using *ImageJ*. Subsequently, Cellpose[128] was used to segment individual outer hair cells (OHC) into regions of interest (ROIs). The mean fluorescence intensity of each OHC was then quantified and normalized to the average fluorescence intensity level of the corresponding control OHCs treated with AM1-43 (4 μM) in L15 and 2% DMSO.

AUTHOR CONTRIBUTIONS

N.A. generated AlphaFold models; P.S. and D.R. performed molecular dynamics simulations to relax the models; D.R., C.M.G., W.G., P.S., and P.D. analyzed the MD simulation data; C.M.G. carried out virtual screening and MM-GBSA calculations, P.D., C.M.G and D.R. performed virtual screening, MM-GBSA analysis, and the selection of compound candidates; P.G. and M.M. carried out cochlear tissue culturing and dye-loading experiments, with assistance from P.D.; P.G. performed confocal imaging; P.G. and A.A.I. analyzed the imaging data; P.D., C.M.G., P.G., A.A.I., and D.R. prepared the original draft of the manuscript; P.D., and A.A.I. edited the manuscript and incorporated feedback from all authors. D.R., P.D., and A.A.I. conceived the study, supervised the project, and secured funding; P.D., A.A.I., D.R., and P.G. conceptualized the study and developed methodology. All authors contributed to the final version of the manuscript.

ACKNOWLEDGMENTS

We thank Dr. Angela Ballesteros (NIDCD) for her valuable scientific feedback and critical reading of the manuscript draft, and Carlos Peña-Varas (Universidad de Concepción – Chile) for advice on figures and data visualization. We also thank Dr. Robert Fettiplace, Dr. Anthony Ricci, Dr. Jeffrey Holt, and Dr. Gwenaelle Geleoc for their feedback and suggestions.

FUNDING

This work was supported by NIH NIDCD R01DC020190, R01DC021795, and R01DC017166 to A.A.I, the NIH NIDCD T32 DC000038 Training Grant awarded to G. Géléoc, supporting M.M., as well as Chilean National Research and Development Agency (ANID), Fondecyt 1220656, 1230446, FOVI210027 and FOVI240021 to D.R. The funders had no role in study design, data collection and analysis, decision to publish, or preparation of the manuscript.

DATA AVAILABILITY

The PDB file containing the coordinates of the simulated MET channel complex, and the 3D-pharmacophores used in this study are available for download from the Ramirez Lab Github repository: https://github.com/ramirezlab/Drug-design-targeting-TMC1.

ETHICS DECLARATIONS

Competing interests

Authors declare that they have no competing financial and/or non-financial interests in relation to this work.

REFERENCES

1. Angeli, S., Lin, X. & Liu, X. Z. Genetics of Hearing and Deafness. *Anat. Rec. Hoboken NJ 2007* **295**, 1812–1829 (2012).
2. Bitner-Glindzicz, M. Hereditary deafness and phenotyping in humans. *Br. Med. Bull.* **63**, 73–94 (2002).
3. Cornejo-Sanchez, D. M. *et al.* Rare-variant association analysis reveals known and new age-related hearing loss genes. *Eur. J. Hum. Genet.* **31**, 638–647 (2023).
4. Eileen, D. Noise and Hearing Loss: A Review. *J Sch Health* **5**, (2007).
5. Kros, C. J. & Steyger, P. S. Aminoglycoside- and Cisplatin-Induced Ototoxicity: Mechanisms and Otoprotective Strategies. *Cold Spring Harb. Perspect. Med.* **9**, a033548 (2019).
6. Wang, X. *et al.* Cisplatin-induced ototoxicity: From signaling network to therapeutic targets. *Biomed. Pharmacother.* **157**, 114045 (2023).
7. Le, T. A. *et al.* Aminoglycoside-Related Nephrotoxicity and Ototoxicity in Clinical Practice: A Review of Pathophysiological Mechanism and Treatment Options. *Adv. Ther.* **40**, 1357–1365 (2023).
8. Rybak, L. P., Ramkumar, V. & Mukherjea, D. Ototoxicity of Non-aminoglycoside Antibiotics. *Front. Neurol.* **12**, 652674 (2021).
9. O'Sullivan, M. E. *et al.* Dissociating antibacterial from ototoxic effects of gentamicin C-subtypes. *Proc. Natl. Acad. Sci. U. S. A.* **117**, 32423–32432 (2020).
10. Huth, M. E., Ricci, A. J. & Cheng, A. G. Mechanisms of Aminoglycoside Ototoxicity and Targets of Hair Cell Protection. *Int. J. Otolaryngol.* **2011**, 937861 (2011).
11. Bitner-Glindzicz, M. & Rahman, S. Ototoxicity caused by aminoglycosides. *BMJ* **335**, 784–785 (2007).
12. Fischel-Ghodsian, N. Genetic factors in aminoglycoside toxicity. *Pharmacogenomics* **6**, 27–36 (2005).
13. Zhao, H. *et al.* Maternally inherited aminoglycoside-induced and nonsyndromic deafness is associated with the novel C1494T mutation in the mitochondrial 12S rRNA gene in a large Chinese family. *Am. J. Hum. Genet.* **74**, 139–152 (2004).
14. Rybak, L. P. & Ramkumar, V. Ototoxicity. *Kidney Int.* **72**, 931–935 (2007).
15. Steyger, P. S. Mechanisms of Ototoxicity and Otoprotection. *Otolaryngol. Clin. North Am.* **54**, 1101–1115 (2021).
16. Vu, A. A. *et al.* Integrity and Regeneration of Mechanotransduction Machinery Regulate Aminoglycoside Entry and Sensory Cell Death. *PLoS ONE* **8**, e54794 (2013).
17. Marcotti, W., Van Netten, S. M. & Kros, C. J. The aminoglycoside antibiotic dihydrostreptomycin rapidly enters mouse outer hair cells through the mechano-electrical transducer channels. *J. Physiol.* **567**, 505–521 (2005).
18. Pan, B. *et al.* TMC1 Forms the Pore of Mechanosensory Transduction Channels in Vertebrate Inner Ear Hair Cells. *Neuron* **99**, 736-753.e6 (2018).
19. Kirkwood, N. K. *et al.* d-Tubocurarine and Berbamine: Alkaloids That Are Permeant Blockers of the Hair Cell's Mechano-Electrical Transducer Channel and Protect from Aminoglycoside Toxicity. *Front. Cell. Neurosci.* **11**, (2017).
20. Alharazneh, A. *et al.* Functional Hair Cell Mechanotransducer Channels Are Required for Aminoglycoside Ototoxicity. *PLOS ONE* **6**, e22347 (2011).
21. Giese, A. P. J. *et al.* Complexes of vertebrate TMC1/2 and CIB2/3 proteins form hair-cell mechanotransduction cation channels. *eLife* **12**, (2023).
22. Ohmori, H. Mechano-electrical transduction currents in isolated vestibular hair cells of the chick. *J. Physiol.* **359**, 189–217 (1985).
23. Kazmierczak, P. *et al.* Cadherin 23 and protocadherin 15 interact to form tip-link filaments in sensory hair cells. *Nature* **449**, 87–91 (2007).
24. Kachar, B., Parakkal, M., Kurc, M., Zhao, Y. & Gillespie, P. G. High-resolution structure of hair-cell tip links. *Proc. Natl. Acad. Sci. U. S. A.* **97**, 13336–13341 (2000).
25. Jaiganesh, A. *et al.* Zooming in on Cadherin-23: Structural Diversity and Potential Mechanisms of Inherited Deafness. *Structure* **26**, 1210-1225.e4 (2018).
26. Siemens, J. *et al.* Cadherin 23 is a component of the tip link in hair-cell stereocilia. *Nature* **428**, 950–955 (2004).

27. Dionne, G. *et al.* Mechanotransduction by PCDH15 Relies on a Novel cis-Dimeric Architecture. *Neuron* **99**, 480-492.e5 (2018).
28. Choudhary, D. *et al.* Structural determinants of protocadherin-15 mechanics and function in hearing and balance perception. *Proc. Natl. Acad. Sci.* **117**, 24837–24848 (2020).
29. Ahmed, Z. M. *et al.* The tip-link antigen, a protein associated with the transduction complex of sensory hair cells, is protocadherin-15. *J Neurosci* **26**, 7022–7034 (2006).
30. Maeda, R. *et al.* Tip-link protein protocadherin 15 interacts with transmembrane channel-like proteins TMC1 and TMC2. *Proc. Natl. Acad. Sci. U. S. A.* **111**, 12907–12912 (2014).
31. Mulhall, E. M. *et al.* Single-molecule force spectroscopy reveals the dynamic strength of the hair-cell tip-link connection. *Nat. Commun.* **12**, 849 (2021).
32. Arora, N. *et al.* Emergence of slip-ideal-slip behavior in tip-links serve as force filters of sound in hearing. *Nat. Commun.* **15**, 1595 (2024).
33. Kenyon, E. J. *et al.* Identification of a series of hair-cell MET channel blockers that protect against aminoglycoside-induced ototoxicity. *JCI Insight* **6**, e145704 (2021).
34. Kitcher, S. R. *et al.* ORC-13661 protects sensory hair cells from aminoglycoside and cisplatin ototoxicity. *JCI Insight* **4**, (2019).
35. Nekrassov, V. & Sitges, M. Vinpocetine protects from aminoglycoside antibiotic-induced hearing loss in guinea pig in vivo. *Brain Res.* **868**, 222–229 (2000).
36. Chowdhury, S. *et al.* Phenotypic Optimization of Urea–Thiophene Carboxamides To Yield Potent, Well Tolerated, and Orally Active Protective Agents against Aminoglycoside-Induced Hearing Loss. *J. Med. Chem.* **61**, 84–97 (2018).
37. Ou, H. C. *et al.* Identification of FDA-Approved Drugs and Bioactives that Protect Hair Cells in the Zebrafish (Danio rerio) Lateral Line and Mouse (Mus musculus) Utricle. *J. Assoc. Res. Otolaryngol.* **10**, 191–203 (2009).
38. Vlasits, A. L., Simon, J. A., Raible, D. W., Rubel, E. W. & Owens, K. N. Screen of FDA-approved drug library reveals compounds that protect hair cells from aminoglycosides and cisplatin. *Hear. Res.* **294**, 153–165 (2012).
39. Breglio, A. M. *et al.* Cisplatin is retained in the cochlea indefinitely following chemotherapy. *Nat. Commun.* **8**, 1654 (2017).
40. Guo, J., Chai, R., Li, H. & Sun, S. Protection of Hair Cells from Ototoxic Drug-Induced Hearing Loss. in *Hearing Loss: Mechanisms, Prevention and Cure* (eds. Li, H. & Chai, R.) 17–36 (Springer, Singapore, 2019). doi:10.1007/978-981-13-6123-4_2.
41. Hsieh, C.-Y. *et al.* Otoprotection against aminoglycoside- and cisplatin-induced ototoxicity focusing on the upstream drug uptake pathway. *J. Chin. Med. Assoc.* **87**, (2024).
42. O'Sullivan, M. E. & Cheng, A. G. Mind Your Ears: A New Antidote to Aminoglycoside Toxicity? *J. Med. Chem.* **61**, 81–83 (2018).
43. Lee, J., Fernandez, K. & Cunningham, L. L. Hear and Now: Ongoing Clinical Trials to Prevent Drug-Induced Hearing Loss. *Annu. Rev. Pharmacol. Toxicol.* **64**, 211–230 (2024).
44. FDA. FDA approves sodium thiosulfate to reduce the risk of ototoxicity associated with cisplatin in pediatric patients with localized, non-metastatic solid tumors. *FDA* (2024).
45. Brock, P. R. *et al.* Sodium Thiosulfate for Protection from Cisplatin-Induced Hearing Loss. *N. Engl. J. Med.* **378**, 2376–2385 (2018).
46. Safety - There's only one PEDMARK. *PEDMARK® (sodium thiosulfate injection)* https://www.pedmark.com/safety/.
47. Deng, G. & Blakley, B. Reducing Aminoglycoside Ototoxicity. *Univ. Manit.* (2012).
48. Wang, J. *et al.* Local application of sodium thiosulfate prevents cisplatin-induced hearing loss in the guinea pig. *Neuropharmacology* **45**, 380–393 (2003).
49. Schroeder, R. J., Audlin, J., Luo, J. & Nicholas, B. D. Pharmacokinetics of sodium thiosulfate in Guinea pig perilymph following middle ear application. *J. Otol.* **13**, 54–58 (2018).
50. Saito, T., Zhang, Z. J., Manabe, Y., Ohtsubo, T. & Saito, H. The effect of sodium thiosulfate on ototoxicity and pharmacokinetics after cisplatin treatment in guinea pigs. *Eur. Arch. Otorhinolaryngol.* **254**, 281–286 (1997).
51. Berglin, C. E. *et al.* Prevention of cisplatin-induced hearing loss by administration of a thiosulfate-containing gel to the middle ear in a guinea pig model. *Cancer Chemother. Pharmacol.* **68**, 1547–1556 (2011).

52. Dhillon, S. Sodium Thiosulfate: Pediatric First Approval. *Pediatr. Drugs* **25**, 239–244 (2023).
53. O'Reilly, M. *et al.* Design, Synthesis, and Biological Evaluation of a New Series of Carvedilol Derivatives That Protect Sensory Hair Cells from Aminoglycoside-Induced Damage by Blocking the Mechanoelectrical Transducer Channel. *J. Med. Chem.* **62**, 5312–5329 (2019).
54. Kruger, M. *et al.* Natural Bizbenzoquinoline Derivatives Protect Zebrafish Lateral Line Sensory Hair Cells from Aminoglycoside Toxicity. *Front. Cell. Neurosci.* **10**, 83 (2016).
55. Jeong, H. *et al.* Structures of the TMC-1 complex illuminate mechanosensory transduction. *Nature* **610**, 796–803 (2022).
56. Pan, B., Waguespack, J., Schnee, M. E., LeBlanc, C. & Ricci, A. J. Permeation properties of the hair cell mechanotransducer channel provide insight into its molecular structure. *J. Neurophysiol.* **107**, 2408–2420 (2012).
57. Derudas, M. *et al.* Charge and lipophilicity are required for effective block of the hair-cell mechano-electrical transducer channel by FM1-43 and its derivatives. *Front. Cell Dev. Biol.* **11**, 1247324 (2023).
58. Gale, J. E., Marcotti, W., Kennedy, H. J., Kros, C. J. & Richardson, G. P. FM1-43 Dye Behaves as a Permeant Blocker of the Hair-Cell Mechanotransducer Channel. *J. Neurosci.* **21**, 7013–7025 (2001).
59. Meyers, J. R. *et al.* Lighting up the senses: FM1-43 loading of sensory cells through nonselective ion channels. *J. Neurosci. Off. J. Soc. Neurosci.* **23**, 4054–4065 (2003).
60. Gund, P. Three-Dimensional Pharmacophoric Pattern Searching. in *Progress in Molecular and Subcellular Biology (PMSB)* (eds. Hahn, F. E., Kersten, H., Kersten, W. & Szybalski, W.) 117–143 (Springer, Berlin, Heidelberg, 1977). doi:10.1007/978-3-642-66626-1_4.
61. Seidel, T., Schuetz, D. A., Garon, A. & Langer, T. The Pharmacophore Concept and Its Applications in Computer-Aided Drug Design. *Prog. Chem. Org. Nat. Prod.* **110**, 99–141 (2019).
62. Medrano-Soto, A. *et al.* Bioinformatic characterization of the Anoctamin Superfamily of Ca2+-activated ion channels and lipid scramblases. *PLoS ONE* **13**, e0192851 (2018).
63. Hahn, Y., Kim, D. S., Pastan, I. H. & Lee, B. Anoctamin and transmembrane channel-like proteins are evolutionarily related. *Int. J. Mol. Med.* **24**, 51–55 (2009).
64. Structural relationship between the putative hair cell mechanotransduction channel TMC1 and TMEM16 proteins | eLife. https://elifesciences.org/articles/38433.
65. Zhang, M. *et al.* Structure of the mechanosensitive OSCA channels. *Nat. Struct. Mol. Biol.* **25**, 850 (2018).
66. Schaller, D. *et al.* Next generation 3D pharmacophore modeling. *WIREs Comput. Mol. Sci.* **10**, e1468 (2020).
67. Ambure, P., Kar, S. & Roy, K. Pharmacophore mapping-based virtual screening followed by molecular docking studies in search of potential acetylcholinesterase inhibitors as anti-Alzheimer's agents. *Biosystems* **116**, 10–20 (2014).
68. Dixon, S. L., Smondyrev, A. M. & Rao, S. N. PHASE: a novel approach to pharmacophore modeling and 3D database searching. *Chem. Biol. Drug Des.* **67**, 370–372 (2006).
69. Yang, S.-Y. Pharmacophore modeling and applications in drug discovery: challenges and recent advances. *Drug Discov. Today* **15**, 444–450 (2010).
70. Ferreira, L. G., Dos Santos, R. N., Oliva, G. & Andricopulo, A. D. Molecular Docking and Structure-Based Drug Design Strategies. *Molecules* **20**, 13384–13421 (2015).
71. Nada, H. *et al.* Perspective for Discovery of Small Molecule IL-6 Inhibitors through Study of Structure–Activity Relationships and Molecular Docking. *J. Med. Chem.* **66**, 4417–4433 (2023).
72. Ren, F. *et al.* AlphaFold accelerates artificial intelligence powered drug discovery: efficient discovery of a novel CDK20 small molecule inhibitor. *Chem. Sci.* **14**, 1443–1452 (2023).
73. Dutt, M. *et al.* Drug repurposing for Mpox: Discovery of small molecules as potential inhibitors against DNA-dependent RNA polymerase using molecular modeling approach. *J. Cell. Biochem.* **124**, 701–715 (2023).
74. Peitzika, S.-C. & Pontiki, E. A Review on Recent Approaches on Molecular Docking Studies of Novel Compounds Targeting Acetylcholinesterase in Alzheimer Disease. *Molecules* **28**, 1084 (2023).
75. Asiamah, I., Obiri, S. A., Tamekloe, W., Armah, F. A. & Borquaye, L. S. Applications of molecular docking in natural products-based drug discovery. *Sci. Afr.* **20**, e01593 (2023).
76. Agu, P. C. *et al.* Molecular docking as a tool for the discovery of molecular targets of nutraceuticals in diseases management. *Sci. Rep.* **13**, 13398 (2023).

77. Kitchen, D. B., Decornez, H., Furr, J. R. & Bajorath, J. Docking and scoring in virtual screening for drug discovery: methods and applications. *Nat. Rev. Drug Discov.* **3**, 935–949 (2004).
78. Malkaje, S., Srinivasa, M. G., Deshpande N, S., Navada, S., & Revanasiddappa BC. An In-silico Approach: Design, Homology Modeling, Molecular Docking, MM/GBSA Simulations, and ADMET Screening of Novel 1,3,4-oxadiazoles as PLK1inhibitors. *Curr. Drug Res. Rev. Former. Curr. Drug Abuse Rev.* **15**, 88–100 (2023).
79. Basnet, S., Ghimire, M. P., Lamichhane, T. R., Adhikari, R. & Adhikari, A. Identification of potential human pancreatic α-amylase inhibitors from natural products by molecular docking, MM/GBSA calculations, MD simulations, and ADMET analysis. *PLOS ONE* **18**, e0275765 (2023).
80. Singh, A. P., Ahmad, S., Raza, K. & Gautam, H. K. Computational screening and MM/GBSA-based MD simulation studies reveal the high binding potential of FDA-approved drugs against Cutibacterium acnes sialidase. *J. Biomol. Struct. Dyn.* **0**, 1–11 (2023).
81. Ramírez, D. *et al.* Discovery of Novel TASK-3 Channel Blockers Using a Pharmacophore-Based Virtual Screening. *Int. J. Mol. Sci.* **20**, 4014 (2019).
82. Ramírez, D. *et al.* 5-(Indol-2-yl)pyrazolo[3,4-b]pyridines as a New Family of TASK-3 Channel Blockers: A Pharmacophore-Based Regioselective Synthesis. *Molecules* **26**, 3897 (2021).
83. Gálvez, J. *et al.* Design, facile synthesis, and evaluation of novel spiro- and pyrazolo[1,5-c]quinazolines as cholinesterase inhibitors: Molecular docking and MM/GBSA studies. *Comput. Biol. Chem.* **74**, 218–229 (2018).
84. De-la-Torre, P. *et al.* A Novel Class of Selective Acetylcholinesterase Inhibitors: Synthesis and Evaluation of (E)-2-(Benzo[d]thiazol-2-yl)-3-heteroarylacrylonitriles. *Molecules* **17**, 12072–12085 (2012).
85. Akyuz, N. *et al.* Mechanical gating of the auditory transduction channel TMC1 involves the fourth and sixth transmembrane helices. *Sci. Adv.* **8**, eabo1126.
86. Hou, T., Wang, J., Li, Y. & Wang, W. Assessing the Performance of the MM/PBSA and MM/GBSA Methods. 1. The Accuracy of Binding Free Energy Calculations Based on Molecular Dynamics Simulations. *J. Chem. Inf. Model.* **51**, 69–82 (2011).
87. Zhang, X. *et al.* Cepharanthine, a novel selective ANO1 inhibitor with potential for lung adenocarcinoma therapy. *Biochim. Biophys. Acta BBA - Mol. Cell Res.* **1868**, 119132 (2021).
88. Beurg, M. *et al.* New Tmc1 Deafness Mutations Impact Mechanotransduction in Auditory Hair Cells. *J. Neurosci.* **41**, 4378–4391 (2021).
89. Murthy, S. E. *et al.* OSCA/TMEM63 are an evolutionarily conserved family of mechanically activated ion channels. *eLife* **7**, e41844 (2018).
90. Walujkar, S. *et al.* In Silico Electrophysiology of Inner-Ear Mechanotransduction Channel TMC1 Models. 2021.09.17.460860 Preprint at https://doi.org/10.1101/2021.09.17.460860 (2021).
91. Maestro, Schrödinger. Schrödinger (2021).
92. Shukla, R. & Tripathi, T. Molecular Dynamics Simulation of Protein and Protein–Ligand Complexes. in *Computer-Aided Drug Design* (ed. Singh, D. B.) 133–161 (Springer, Singapore, 2020). doi:10.1007/978-981-15-6815-2_7.
93. Law, R. J. *et al.* Membrane protein structure quality in molecular dynamics simulation. *J. Mol. Graph. Model.* **24**, 157–165 (2005).
94. Arnittali, M., Rissanou, A. N. & Harmandaris, V. Structure Of Biomolecules Through Molecular Dynamics Simulations. *Procedia Comput. Sci.* **156**, 69–78 (2019).
95. Shi, S. *et al.* Molecular mechanism of ion channel protein TMEM16A regulated by natural product of narirutin for lung cancer adjuvant treatment. *Int. J. Biol. Macromol.* **223**, 1145–1157 (2022).
96. Zamri, M. H. B., Ujihara, Y., Nakamura, M., Mofrad, M. R. K. & Sugita, S. Decoding the Effect of Hydrostatic Pressure on TRPV1 Lower-Gate Conformation by Molecular-Dynamics Simulation. *Int. J. Mol. Sci.* **23**, 7366 (2022).
97. Smart, O. S., Neduvelil, J. G., Wang, X., Wallace, B. A. & Sansom, M. S. HOLE: a program for the analysis of the pore dimensions of ion channel structural models. *J. Mol. Graph.* **14**, 354–60, 376 (1996).
98. Owens, K. N. *et al.* Identification of Genetic and Chemical Modulators of Zebrafish Mechanosensory Hair Cell Death. *PLOS Genet.* **4**, e1000020 (2008).
99. Majumder, P., Moore, P. A., Richardson, G. P. & Gale, J. E. Protecting Mammalian Hair Cells from Aminoglycoside-Toxicity: Assessing Phenoxybenzamine's Potential. *Front. Cell. Neurosci.* **11**, (2017).

100. Zhou, Y., Di, B. & Niu, M.-M. Structure-Based Pharmacophore Design and Virtual Screening for Novel Tubulin Inhibitors with Potential Anticancer Activity. *Molecules* **24**, 3181 (2019).
101. Zhao, S. *et al.* Ligand-based pharmacophore modeling, virtual screening and biological evaluation to identify novel TGR5 agonists. *RSC Adv.* **11**, 9403–9409.
102. Ntie-Kang, F. *et al.* Pharmacophore modeling and in silico toxicity assessment of potential anticancer agents from African medicinal plants. *Drug Des. Devel. Ther.* **10**, 2137–2154 (2016).
103. Vyas, V. K., Ghate, M. & Goel, A. Pharmacophore modeling, virtual screening, docking and in silico ADMET analysis of protein kinase B (PKB β) inhibitors. *J. Mol. Graph. Model.* **42**, 17–25 (2013).
104. Zaccagnini, L. *et al.* Identification of novel fluorescent probes preventing PrPSc replication in prion diseases. *Eur. J. Med. Chem.* **127**, 859–873 (2017).
105. Irwin, J. J. & Shoichet, B. K. ZINC – A Free Database of Commercially Available Compounds for Virtual Screening. *J. Chem. Inf. Model.* **45**, 177–182 (2005).
106. MicroSource Discovery Systems, Inc. - The US Drug Collection. http://www.msdiscovery.com/usdrug.html.
107. Koes, D. R. & Camacho, C. J. ZINCPharmer: pharmacophore search of the ZINC database. *Nucleic Acids Res.* **40**, W409-414 (2012).
108. Zhang, M. *et al.* Pharmacophore Modeling, Synthesis, and Antibacterial Evaluation of Chalcones and Derivatives. *ACS Omega* **3**, 18343–18360 (2018).
109. Life Science: LigPrep. *Schrödinger* https://newsite.schrodinger.com/platform/products/ligprep/.
110. Shelley, J. C. *et al.* Epik: a software program for pKaprediction and protonation state generation for drug-like molecules. *J. Comput. Aided Mol. Des.* **21**, 681–691 (2007).
111. Epik, S. Protein Preparation Wizard. Epik: Schrödinger, LLC, New York, NY. Schrödinger, LLC. (2019).
112. Vélez-Ortega, A. C., Freeman, M. J., Indzhykulian, A. A., Grossheim, J. M. & Frolenkov, G. I. Mechanotransduction current is essential for stability of the transducing stereocilia in mammalian auditory hair cells. *eLife* **6**, e24661.
113. Rüsch, A., Kros, C. J. & Richardson, G. P. Block by amiloride and its derivatives of mechano-electrical transduction in outer hair cells of mouse cochlear cultures. *J. Physiol.* **474**, 75–86 (1994).
114. Ballesteros, A. & Swartz, K. J. Regulation of membrane homeostasis by TMC1 mechanoelectrical transduction channels is essential for hearing. *Sci. Adv.* **8**, eabm5550 (2022).
115. Corns, L. F., Johnson, S. L., Kros, C. J. & Marcotti, W. Tmc1 Point Mutation Affects Ca2+ Sensitivity and Block by Dihydrostreptomycin of the Mechanoelectrical Transducer Current of Mouse Outer Hair Cells. *J. Neurosci.* **36**, 336–349 (2016).
116. Kroese, A. B. A., Das, A. & Hudspeth, A. J. Blockage of the transduction channels of hair cells in the bullfrog's sacculus by aminoglycoside antibiotics. *Hear. Res.* **37**, 203–217 (1989).
117. Friesner, R. A. *et al.* Glide: a new approach for rapid, accurate docking and scoring. 1. Method and assessment of docking accuracy. *J. Med. Chem.* **47**, 1739–1749 (2004).
118. Vreugde, S. *et al.* Beethoven, a mouse model for dominant, progressive hearing loss DFNA36. *Nat. Genet.* **30**, 257–258 (2002).
119. Fettiplace, R., Furness, D. N. & Beurg, M. The conductance and organization of the TMC1-containing mechanotransducer channel complex in auditory hair cells. *Proc. Natl. Acad. Sci.* **119**, e2210849119 (2022).
120. Corey, D. P., Akyuz, N. & Holt, J. R. Function and Dysfunction of TMC Channels in Inner Ear Hair Cells. *Cold Spring Harb. Perspect. Med.* **9**, a033506 (2019).
121. Hansen, F. A. & Pedersen-Bjergaard, S. Electromembrane extraction of streptomycin from biological fluids. *J. Chromatogr. A* **1639**, 461915 (2021).
122. Blundell, C. D., Packer, M. J. & Almond, A. Quantification of free ligand conformational preferences by NMR and their relationship to the bioactive conformation. *Bioorg. Med. Chem.* **21**, 4976–4987 (2013).
123. Rácz, A., Bajusz, D. & Héberger, K. Life beyond the Tanimoto coefficient: similarity measures for interaction fingerprints. *J. Cheminformatics* **10**, 48 (2018).
124. Beurg, M., Goldring, A. C. & Fettiplace, R. The effects of Tmc1 Beethoven mutation on mechanotransducer channel function in cochlear hair cells. *J. Gen. Physiol.* **146**, 233–243 (2015).

125. Beurg, M., Barlow, A., Furness, D. N. & Fettiplace, R. A Tmc1 mutation reduces calcium permeability and expression of mechanoelectrical transduction channels in cochlear hair cells. *Proc. Natl. Acad. Sci.* **116**, 20743–20749 (2019).
126. Holt, J. R. *et al.* Putting the Pieces Together: the Hair Cell Transduction Complex. *JARO J. Assoc. Res. Otolaryngol.* **22**, 601–608 (2021).
127. Goldring, A. C., Beurg, M. & Fettiplace, R. The contribution of TMC1 to adaptation of mechanoelectrical transduction channels in cochlear outer hair cells. *J. Physiol.* **597**, 5949–5961 (2019).
128. Stringer, C., Wang, T., Michaelos, M. & Pachitariu, M. Cellpose: a generalist algorithm for cellular segmentation. *Nat. Methods* **18**, 100–106 (2021).
129. Ballesteros, A., Fenollar-Ferrer, C. & Swartz, K. J. Structural relationship between the putative hair cell mechanotransduction channel TMC1 and TMEM16 proteins. *eLife* **7**, e38433 (2018).
130. Al-Hosni, R., Ilkan, Z., Agostinelli, E. & Tammaro, P. The pharmacology of the TMEM16A channel: therapeutic opportunities. *Trends Pharmacol. Sci.* **43**, 712–725 (2022).
131. Paulino, C., Kalienkova, V., Lam, A. K. M., Neldner, Y. & Dutzler, R. Activation mechanism of the calcium-activated chloride channel TMEM16A revealed by cryo-EM. *Nature* **552**, 421–425 (2017).
132. Shi, S., Ma, B., Sun, F., Qu, C. & An, H. Theaflavin binds to a druggable pocket of TMEM16A channel and inhibits lung adenocarcinoma cell viability. *J. Biol. Chem.* **297**, (2021).
133. Shi, S. *et al.* Identification of a druggable pocket of the calcium-activated chloride channel TMEM16A in its open state. *J. Biol. Chem.* **299**, 104780 (2023).
134. Jia, Z. & Chen, J. Specific PIP2 binding promotes calcium activation of TMEM16A chloride channels. *Commun. Biol.* **4**, 1–10 (2021).
135. Ballesteros, A. & Swartz, K. J. Dextran Labeling and Uptake in Live and Functional Murine Cochlear Hair Cells. *J. Vis. Exp. JoVE* (2020) doi:10.3791/60769.
136. Farris, H. E., LeBlanc, C. L., Goswami, J. & Ricci, A. J. Probing the pore of the auditory hair cell mechanotransducer channel in turtle. *J. Physiol.* **558**, 769–792 (2004).
137. Zhao, Y. *et al.* A novel DFNA36 mutation in TMC1 orthologous to the Beethoven (Bth) mouse associated with autosomal dominant hearing loss in a Chinese family. *PloS One* **9**, e97064 (2014).
138. De-la-Torre, P., Choudhary, D., Araya-Secchi, R., Narui, Y. & Sotomayor, M. A Mechanically Weak Extracellular Membrane-Adjacent Domain Induces Dimerization of Protocadherin-15. *Biophys. J.* **115**, 2368–2385 (2018).
139. Farhadi, M., Razmara, E., Balali, M., Hajabbas Farshchi, Y. & Falah, M. How Transmembrane Inner Ear (TMIE) plays role in the auditory system: A mystery to us. *J. Cell. Mol. Med.* **25**, 5869–5883 (2021).
140. Kurima, K. *et al.* TMC1 and TMC2 Localize at the Site of Mechanotransduction in Mammalian Inner Ear Hair Cell Stereocilia. *Cell Rep.* **12**, 1606–1617 (2015).
141. Ratzan, E. M. *et al.* TMC function, dysfunction, and restoration in mouse vestibular organs. *Front. Neurol.* **15**, (2024).
142. Kawashima, Y. *et al.* Mechanotransduction in mouse inner ear hair cells requires transmembrane channel–like genes. *J. Clin. Invest.* **121**, 4796–4809 (2011).
143. Clark, S., Jeong, H., Posert, R., Goehring, A. & Gouaux, E. The structure of the Caenorhabditis elegans TMC-2 complex suggests roles of lipid-mediated subunit contacts in mechanosensory transduction. *Proc. Natl. Acad. Sci. U. S. A.* **121**, e2314096121 (2024).
144. Guo, Z. *et al.* Identification of Protein–Ligand Binding Sites by the Level-Set Variational Implicit-Solvent Approach. *J. Chem. Theory Comput.* **11**, 753–765 (2015).
145. Holt, J. R., Fettiplace, R. & Müller, U. Sensory transduction in auditory hair cells—PIEZOs can't touch this. *J. Gen. Physiol.* **156**, e202413585 (2024).
146. Mirdita, M., Ovchinnikov, S. & Steinegger, M. ColabFold - Making protein folding accessible to all. 2021.08.15.456425 Preprint at https://doi.org/10.1101/2021.08.15.456425 (2021).
147. Giese, A. P. J. *et al.* CIB2 interacts with TMC1 and TMC2 and is essential for mechanotransduction in auditory hair cells. *Nat. Commun.* **8**, 43 (2017).
148. Liang, X. *et al.* CIB2 and CIB3 are auxiliary subunits of the mechanotransduction channel of hair cells. *Neuron* **109**, 2131-2149.e15 (2021).
149. Jacobson, M. P., Friesner, R. A., Xiang, Z. & Honig, B. On the Role of the Crystal Environment in Determining Protein Side-chain Conformations. *J. Mol. Biol.* **320**, 597–608 (2002).

150. Olsson, M. H. M., Søndergaard, C. R., Rostkowski, M. & Jensen, J. H. PROPKA3: Consistent Treatment of Internal and Surface Residues in Empirical pKa Predictions. *J. Chem. Theory Comput.* **7**, 525–537 (2011).
151. Bowers, K. J. *et al.* Scalable Algorithms for Molecular Dynamics Simulations on Commodity Clusters. in *SC '06: Proceedings of the 2006 ACM/IEEE Conference on Supercomputing* 43–43 (2006). doi:10.1109/SC.2006.54.
152. Lu, C. *et al.* OPLS4: Improving Force Field Accuracy on Challenging Regimes of Chemical Space. *J. Chem. Theory Comput.* **17**, 4291–4300 (2021).
153. Gallego-Yerga, L. *et al.* Application of ensemble pharmacophore-based virtual screening to the discovery of novel antimitotic tubulin inhibitors. *Comput. Struct. Biotechnol. J.* **19**, 4360–4372 (2021).
154. Martyna, G. J., Tobias, D. J. & Klein, M. L. Constant pressure molecular dynamics algorithms. *J. Chem. Phys.* **101**, 4177–4189 (1994).
155. Humphrey, W., Dalke, A. & Schulten, K. VMD: Visual molecular dynamics. *J. Mol. Graph.* **14**, 33–38 (1996).
156. DeLano, W. L. Pymol. (2002).
157. Gori, D. N. P. *et al.* LIDeB Tools: A Latin American resource of freely available, open-source cheminformatics apps. *Artif. Intell. Life Sci.* **2**, 100049 (2022).
158. Truchon, J.-F. & Bayly, C. I. Evaluating Virtual Screening Methods: Good and Bad Metrics for the "Early Recognition" Problem. *J. Chem. Inf. Model.* **47**, 488–508 (2007).
159. Harder, E. *et al.* OPLS3: A Force Field Providing Broad Coverage of Drug-like Small Molecules and Proteins. *J. Chem. Theory Comput.* **12**, 281–296 (2016).
160. Berthold, M. R. *et al.* KNIME - the Konstanz information miner: version 2.0 and beyond. *ACM SIGKDD Explor. Newsl.* **11**, 26–31 (2009).
161. Structure-Based Virtual Screening Using Phase Workshop Tutorial | Schrödinger. https://www.schrodinger.com/training/structure-based-virtual-screening-using-phase-workshop-tutorial221.
162. Prime, Schrödinger, LLC, New York, NY, USA. (2017).
163. Kaminski, G. A., Friesner, R. A., Tirado-Rives, J. & Jorgensen, W. L. Evaluation and Reparametrization of the OPLS-AA Force Field for Proteins via Comparison with Accurate Quantum Chemical Calculations on Peptides. *J. Phys. Chem. B* **105**, 6474–6487 (2001).
164. Li, J. *et al.* The VSGB 2.0 model: a next generation energy model for high resolution protein structure modeling. *Proteins* **79**, 2794–2812 (2011).
165. Rogers, D. & Hahn, M. Extended-Connectivity Fingerprints. *J. Chem. Inf. Model.* **50**, 742–754 (2010).

FIGURES, FIGURE LEGENDS, AND TABLES

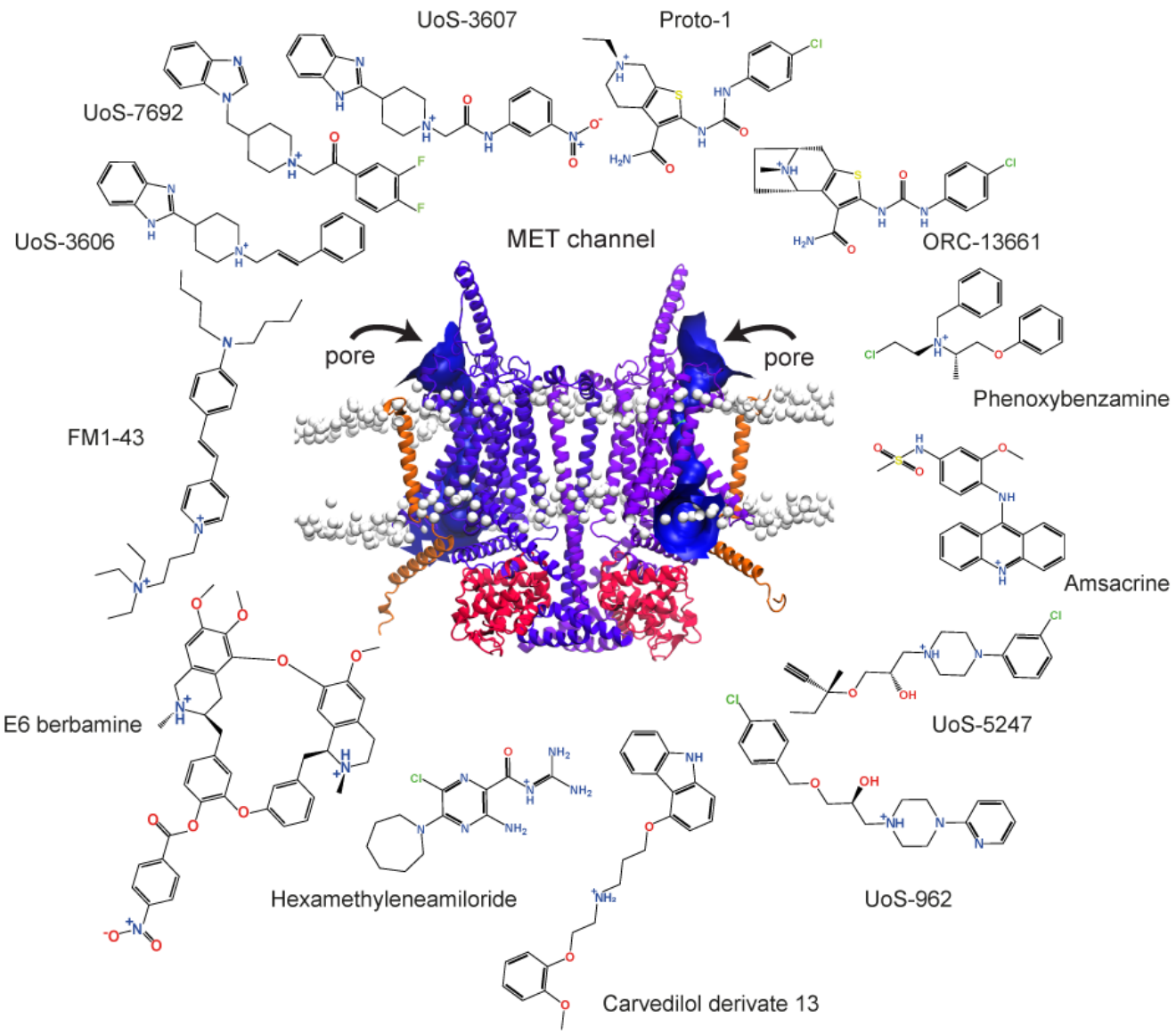

Figure 1. Structural diversity of known MET blockers. Compounds reported to display varied MET channel blocker potencies and AG protection (see *Supp Table 1*). These compounds share a protonatable nitrogen atom and at least one aromatic ring in their structures. Potential protonatable nitrogen atoms are marked with a blue plus sign. Front view a of our dimeric TMC1 model (*purple*) in complex with two protomers of TMIE (*orange*) and two protomers of CIB2 (*red*) proteins. Heads of phospholipids are showed as white beads. Arrows represent the entry site of small molecules via the pores in both TMC1 protomers calculated by HOLE[90] (*blue*). More details about this model are presented in *Figure 2* and in the *Methods* section.

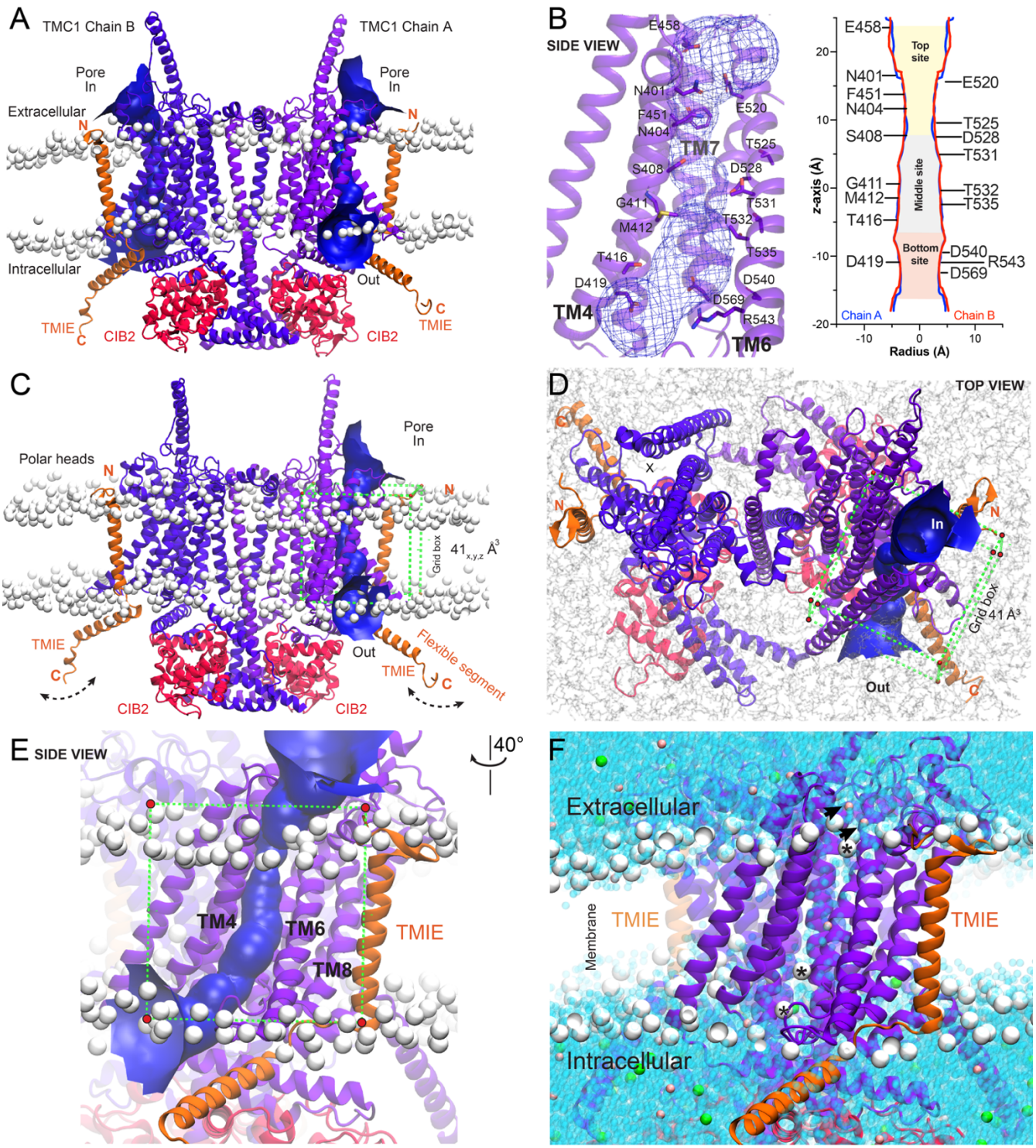

Figure 2. TMC1 modeling and molecular dynamics simulations. We built a dimeric open-like conformation of the TMC1 structure using *AlphaFold2*. **(A)** Front view of a 25 ns frame of the dimeric, equilibrated TMC1 protein in complex with two protomers of TMIE (*orange*) and two protomers of CIB2 (*red*) proteins. The system is embedded in a POPC membrane, with the phosphorus of the phospholipids heads illustrated as white beads. The TMC1 pores of chain A and B are represented by a blue funnel obtained by HOLE[90] analysis. **(B)** Detailed view of the TMC1 pore of chain A, depicting the pore in a mesh representation, and amino acids as purple sticks. The inset depicts the van der Waals radius (Å) of the pore plotted against the distance (Å) along the pore of both TMC1 chains (*z*-axis), obtained by HOLE[90] analysis. Top (*gold*), middle (*light gray*), and bottom (*light red*) sites of the pore are labeled and color-coded according to the most expanded regions of the pore. The zero (0 Å) at the z-axis represents the reference position of the middle site of the TMC1 pore at the center of the plasma membrane. See *Supp Figure 2* for additional details and quantitative analysis . **(C)** Front view of the complex as in panel *a*. The flexible TMIE C-terminal segment is labeled (see *Supp Figure 2*). A 41 Å^3 docking gridbox is represented by green dashed lines with vertices in red circles. **(D)** Top view of the simulated system showing the swapped TMC1 conformation with two pores represented by a blue surface (chain A) and a dashed circle with an X (chain B), respectively. Same gridbox as in panel *c*. **(E)** Zoomed-in side view of chain A from panel *c* showing the gridbox and TM domains forming the pore. **(F)** Zoomed-in side view of the MET complex showing water molecules filling the pore (*blue beads*). K^+ ions are illustrated as pink beads, while Cl^- ions as green beads. K^+ ions visiting the pore are pointed with black arrows. Phospholipids that moved into the pore are indicated by asterisks (see *Supp Figure 5*).

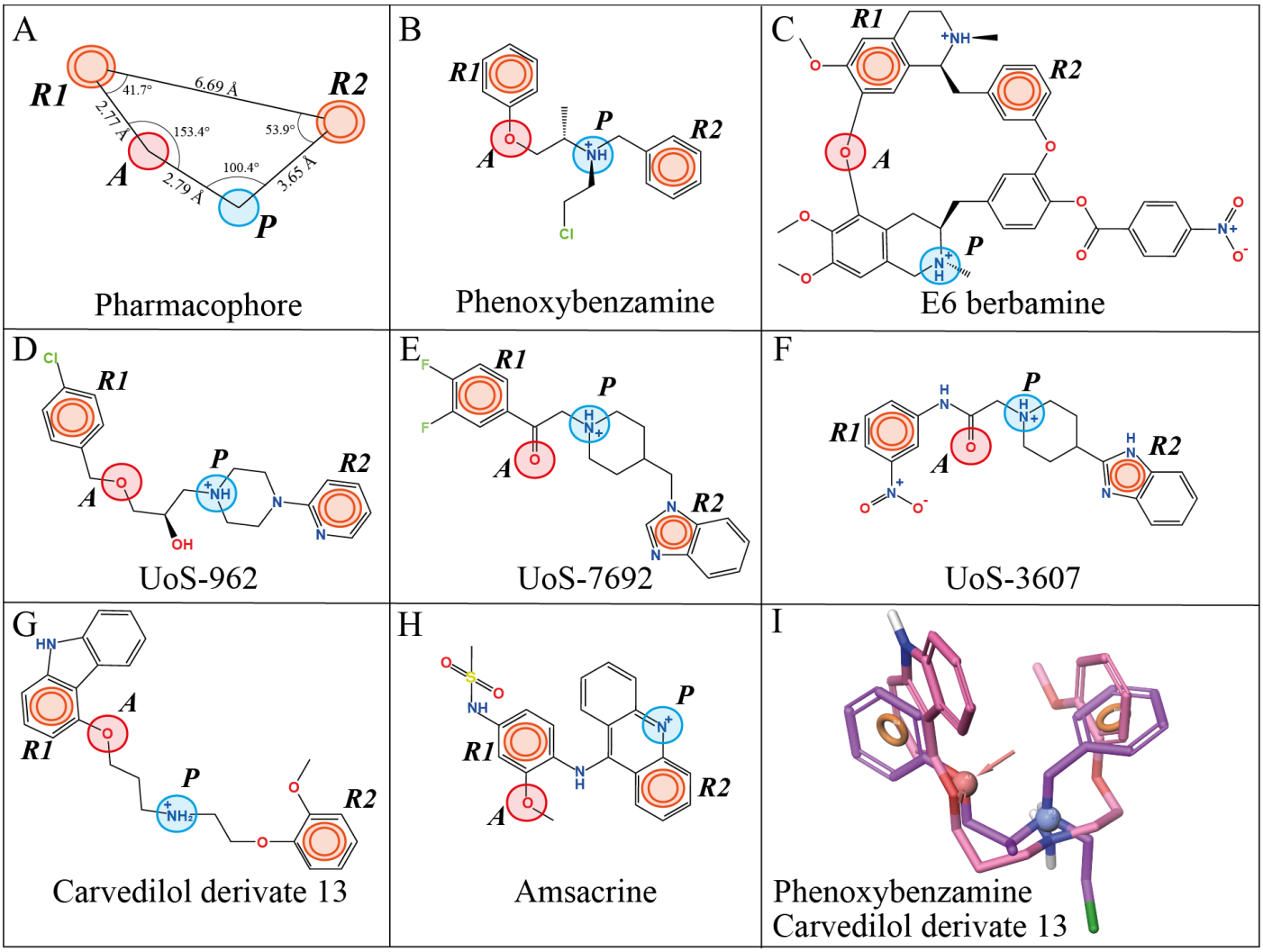

Figure 3. Pharmacophore modeling of 13 known MET channel blockers. **(A)** The APRR four-point pharmacophore model of MET channel modulators show a hydrogen-bond acceptor feature (*A*) in red, two aromatic rings (*R1* and *R2*) in orange, and a positively charged group (*P*) in blue. Distances and angles between the pharmacophoric features are labeled. This model showed the highest *PhaseHypoScore* (APRR = 0.780) matching 7 out of 13 matching blockers. **(B–H)** A 2D-representation of the APRR pharmacophore model with matching compounds. **(I)** Superposed 3D-structures of the MET blockers phenoxybenzamine (*purple*) and carvedilol derivative 13 (*pink*) onto the APRR pharmacophore. These two compounds fit all 10 pharmacophores reported in Table 1 (see also *Supp Table 2*).

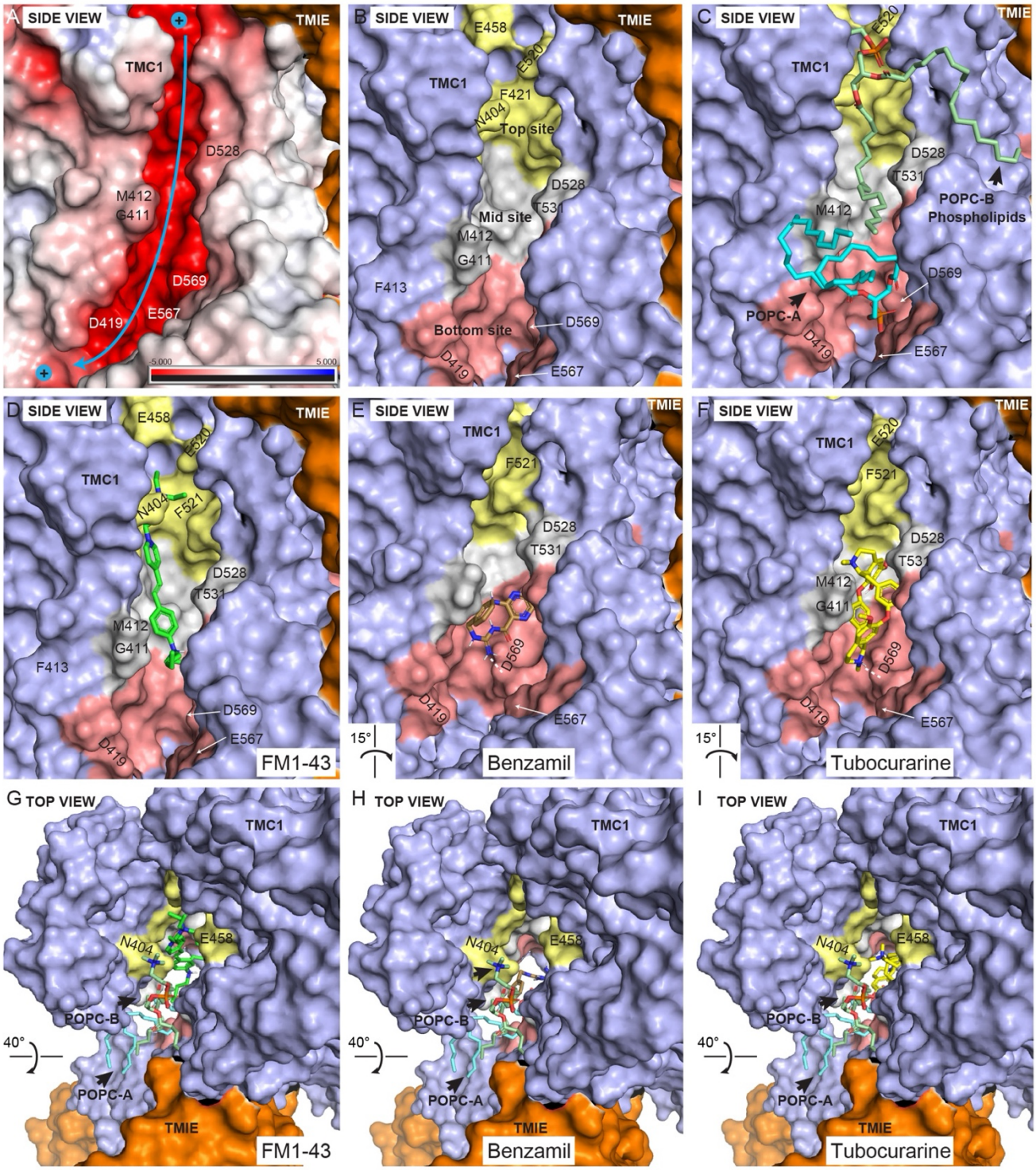

Figure 4. Molecular docking of known blockers within the TMC1 pore cavity. Side view surface representation of TMC1 chain A pore (*light purple*). TMIE is shown as an orange surface, while CIB2 is not displayed for clarity. **(A)** Surface electrostatic potential (calculated by PyMOL) of TMC1 cavity. Electronegative area is highlighted in red, electropositive in blue, and hydrophobic in white. The cavity of TMC1 is highly electronegative with a cation pathway indicated by the *blue arrow*. **(B)** TMC1 pore cavity highlighting 3 ligand-binding sites: top (*gold*), middle (*light gray*), and bottom (*light red*) sites of the pore, color-coded for illustration purposes. Binding at these sites is governed by interactions between the positively charged amine group of the ligands with residues E458 and F451 (*top site*), D528 (*middle site*), and D569 (*bottom site*), as well as hydrophobic and hydrogen bond interactions with other residues within the TMC1 pore cavity. **(C)** Side view, similar to panel *b*, showing the location of two key phospholipids (POPC-A and POPC-B) identified during MD simulations. The polar head of POPC-A points towards the bottom site forming a zwitterionic-like interaction network near D569, key for ligand binding. Additionally, the polar head of POPC-B forms a similar zwitterionic-like network with R523 at the top site (see also *Figure 6* and *Supp. Figure 5*). **(D)** Binding interaction of FM1-43 (*green*) across the top, middle, and near the bottom sites of the pore. **(I)** Binding interaction of benzamil (*brown*) at the bottom site of the pore. Dashed white line represents a hydrogen bond interaction with D569. **(F)** Binding interaction of tubocurarine (*yellow*) at the middle and the bottom sites of the pore. Dashed white line as in panel E. **(G-I)** Top views of FM1-43, benzamil, and tubocurarine showing the location of the ligands and the phospholipid sidewall formed by POPC-A and POPC-B surrounding the ligands. Additional illustrations on interactions are presented in *Figure 6* and *Supp Figure 5*.

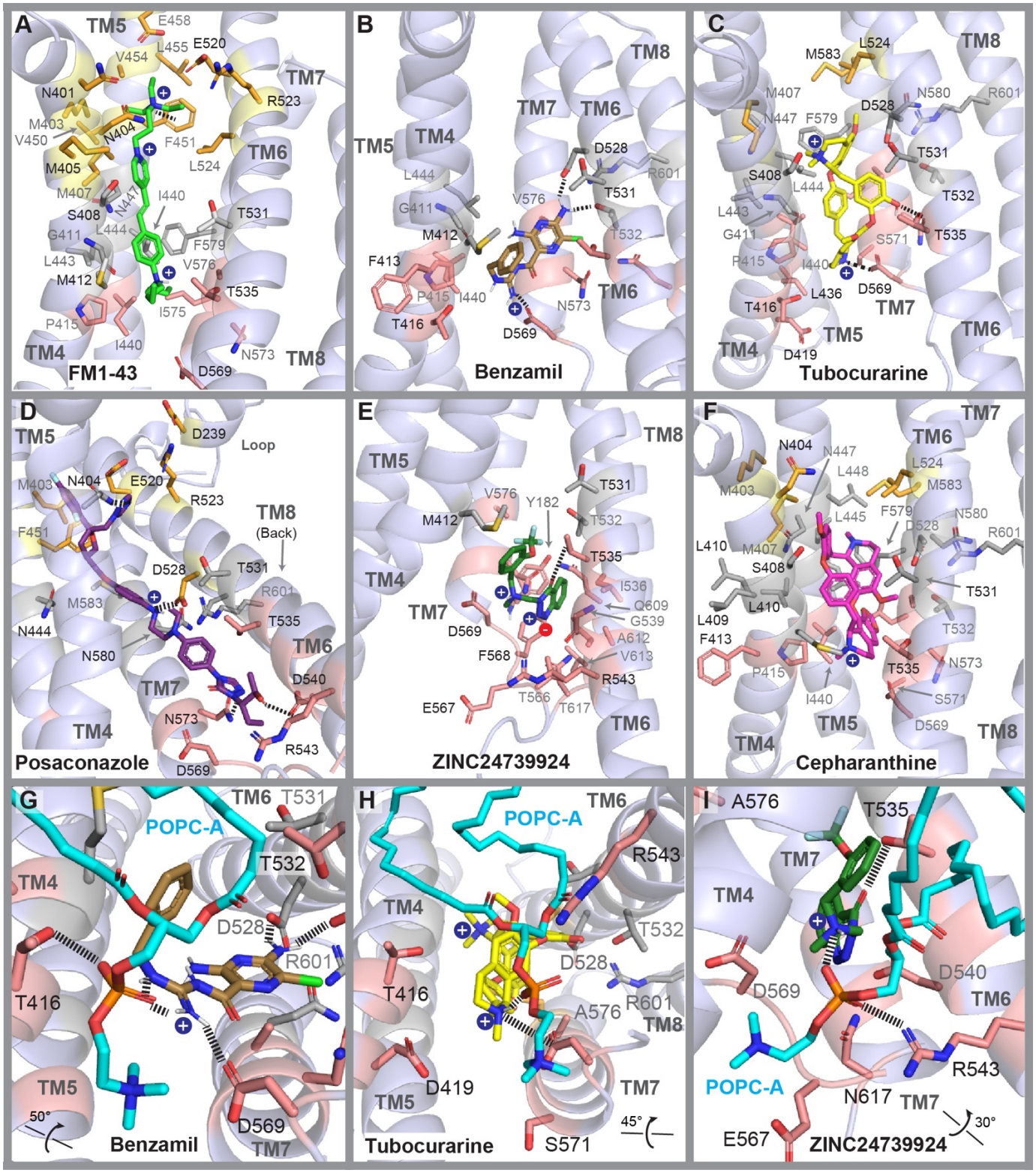

Figure 5. Molecular docking simulations of known and novel TMC1 blockers. Cartoon representation and binding modes of blockers. **(A)** FM1-43 (*green*) within the cavity of TMC1 (*light purple*). **(B)** Benzamil (*brown*). **(C)** Tubocurarine (*yellow*). **(D)** Posaconazole (*dark purple*). **(E)** Compound ZINC24739924 (*green*). **(F)** Cepharanthine (*magenta*). **(G-I)** Bottom view of the ZN3 bottom site with benzamil, tubocurarine, and compound ZINC24739924, respectively. Residues are labeled in *black* and *gray* for their position at the front or at the back of each helix, respectively. The side chains and the backbone residues are colored as in *Figure 4*, according to their location within the top (*gold*), middle (*light gray*), and bottom (*light red*) sites of the TMC1 pore. Residues within 5 Å distance from each blocker are displayed, and key interactions highlighted with black dashed lines. Additional illustrations on interactions are presented in *Supp Figure 5*.

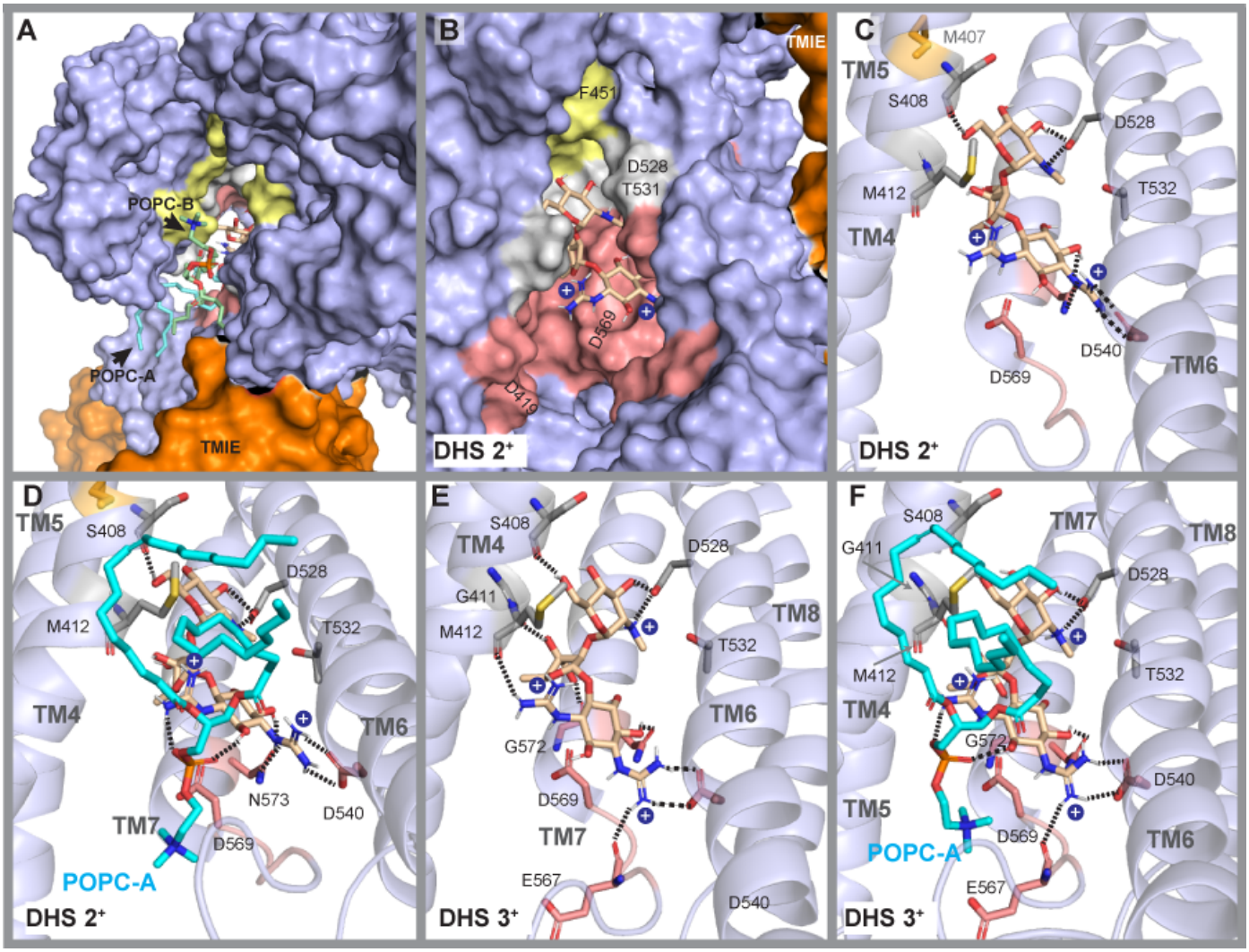

Figure 6. Molecular docking of dihydrostreptomycin (DHS) within the TMC1 pore. Binding interactions following molecular docking and MM-GBSA. Phospholipids are not displayed in some panels to visualize DHS and TMC1 only. Each positively charged nitrogen is shown as a blue bead. Dashed lines represent direct hydrogen bonds or salt-bridge interactions. **(A)** Top view of DHS (2^+) showing the location of the ligand and the phospholipid sidewall formed by POPC-A and POPC-B, surrounding the ligands. **(B)** Side view of DHS (2^+) within the TMC1 pore. Top site (*gold*), middle site (*light gray*), and bottom site (*light red*) are shown. Phospholipids are not displayed for clarity. Binding at these sites is governed by interactions between the positively charged amine and guanidinium groups, as well as the hydroxyl groups of DHS (2^+) with amino acids of the middle and bottom sites. **(C)** Docking pose of DHA (2^+) showing hydrogen bonds between the *N*-methyl-*L*-glucosamine head with the amino acids S408 and D528. The streptose moiety pointed towards TM7, while the guanidinium groups of the streptidine moiety displayed hydrogen bond interactions with N573 and salt bridges with D540. One of the guanidinium groups points to D569 in a region exposed to solvent (*more details in panel d*). **(D)** Bottom view from panel C. Interactions between DHS (2^+), TMC1, and POPC-A within the bottom site of the pore cavity. One guanidinium group displayed interactions with N573 and D540 (*as in panel c*), while the second guanidinium group showed interactions with the polar head of POPC-A. **(E)** Side view of DHS (3^+) within the pore showing interactions similar to DHS (2^+). Additionally, the hydroxyl group of the streptose moiety formed hydrogen bonds with the carbonyl backbone groups of G411 and G572, while the guanidinium groups formed hydrogen bonds with the carbonyl backbone groups of M412 and E567. **(F)** Interactions of DHS (3^+) within the pore and with POPC-A.

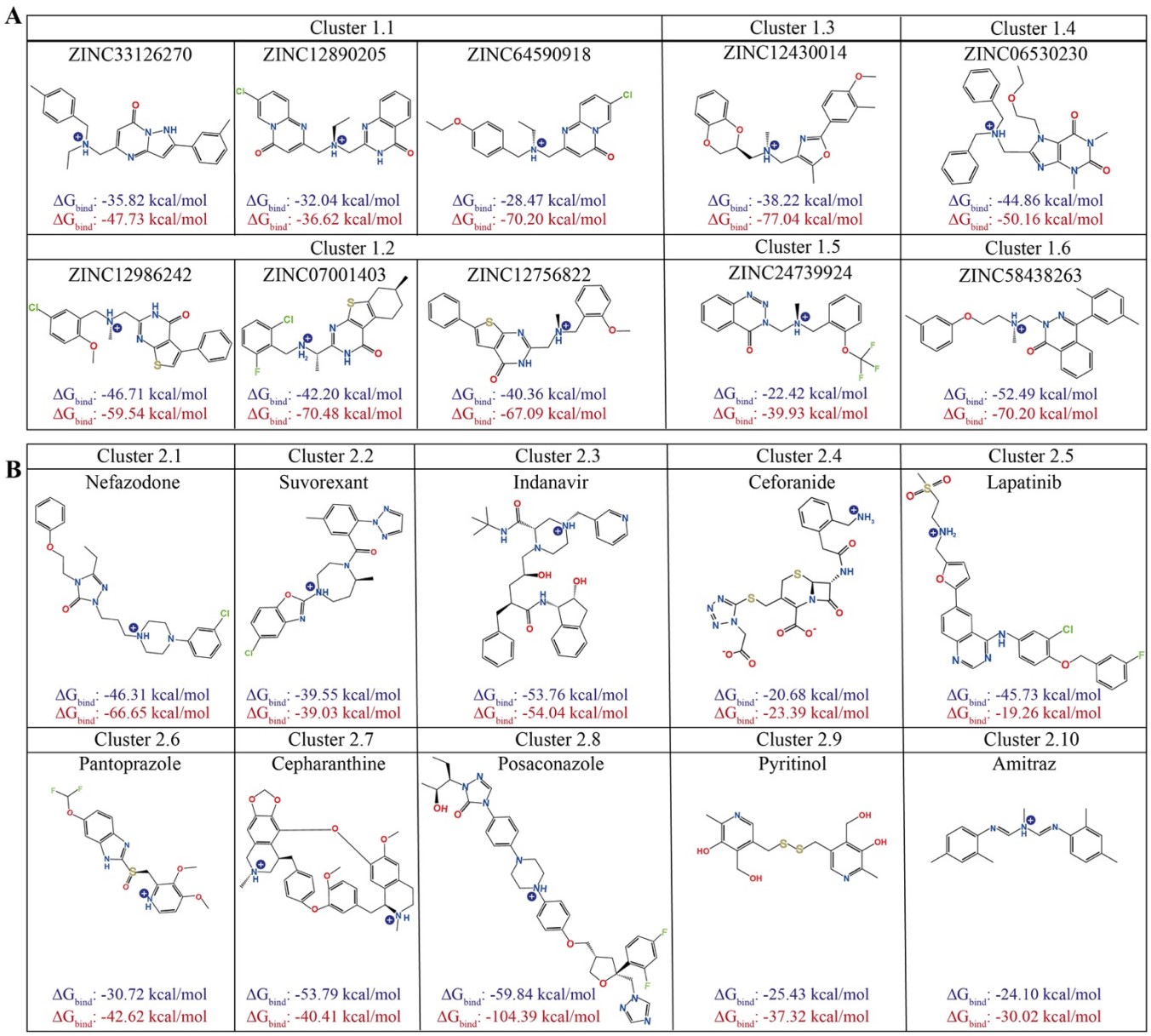

Figure 7. **List of final hits selected for experimental evaluation. (A)** Chemical structures of the 10 selected hits from *Library* 1 (non-FDA-approved). **(B)** Chemical structures of the 10 selected hits from *Library* 2 (FDA-approved drugs). The calculated MM-GBSA ΔG_{bind} energies are shown for all selected hit compounds in blue (without POPCs) and in red (with POPCs), respectively. Compounds were sketched using ChemDraw.

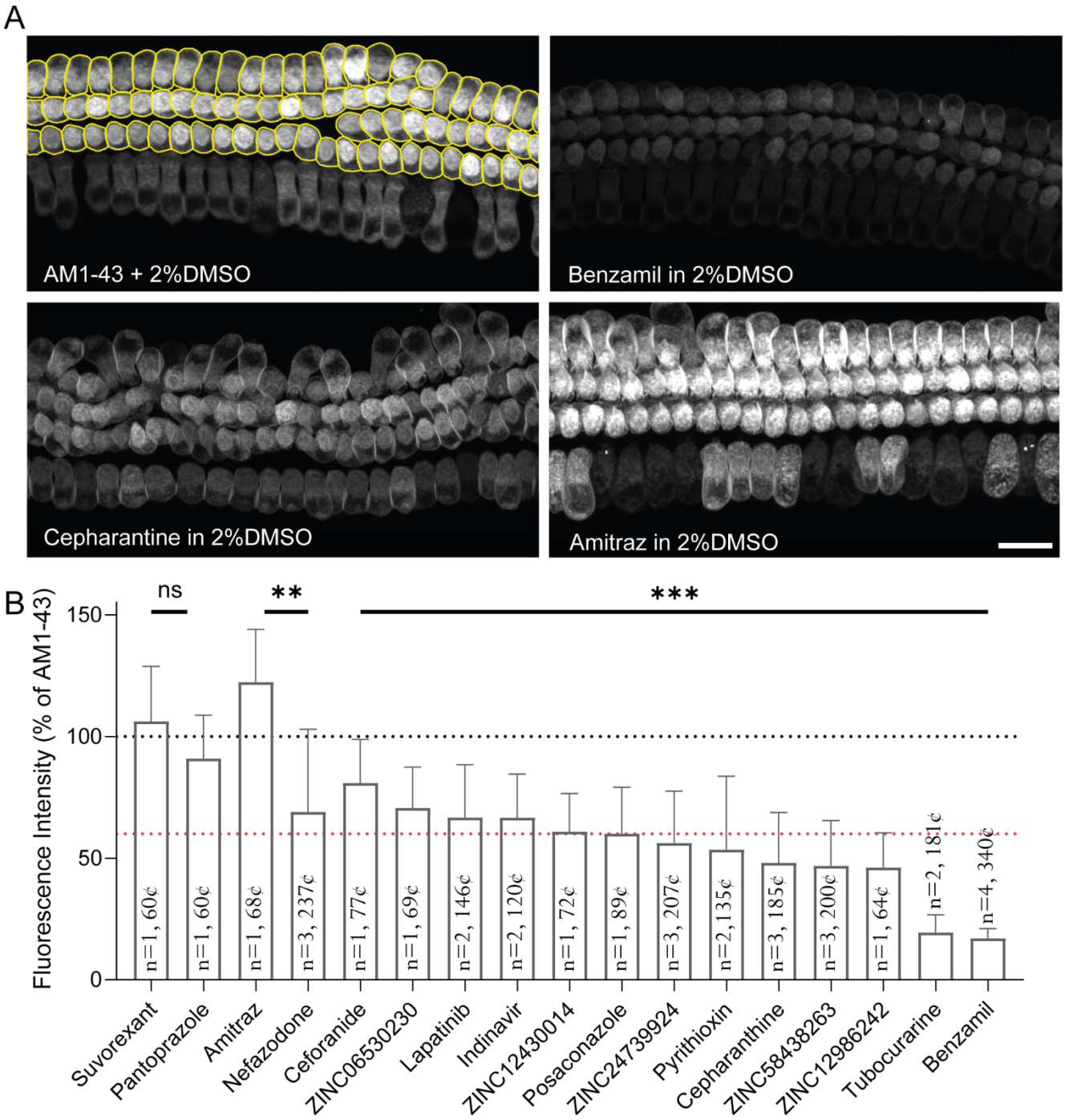

Figure 8. Evaluation of predicted TMC1 modulators in live cochlear hair cells using AM1-43 dye uptake assay. (A) Representative confocal microscopy images of AM1-43 dye loading into hair cells from the middle region of the cochlea. The Cellpose algorithm was used to segment each OHC as individual region of interest (*top left* panel). Dye uptake was reduced by treatment with benzamil (*top right*) and cepharantine (*bottom left*) but increased following treatment with Amitraz (*bottom right*) compared to DMSO-treated controls (*top left*). Scale bar: 15µm. **(B)** Averaged AM1-43 dye uptake by OHCs in cochlear explants treated with 16 commercially available hit compounds normalized to values obtained from DMSO-treated control explants of the same experimental session. The number of experimental sessions and total number of analyzed cells are indicated within the histogram bar. Data are presented as mean ± SD. To compare the average compound fluorescence with the average control levels from the same experimental sessions, the Kruskal-Wallis test followed by Dunn's multiple comparison test was used. $p > 0.5$ (ns); $p < 0.01$(**); $p < 0.001$(***). Individual AM1-43 dye loading intensities across each experimental sessions are reported in *Supp Figure* 8.

Table 1. Pharmacophore models identified by *Phase* and scored by *PhaseHypoScore*[67] (See *Methods*).

Pharmacophore ID	Pharmacophore hypothesis	Number of matching compounds	PhaseHypoScore
ID-1	APRR	7	0.780
ID-2	APR-1	9	0.762
ID-3	APR-2	8	0.759
ID-4	PRR	7	0.698
ID-5	ARR-1	7	0.629
ID-6	ARR-2	9	0.526
ID-7	AHR	7	0.475
ID-8	ARR-3	7	0.418
ID-9	ARR-4	8	0.385
ID-10	HRR	9	0.340

A: Hydrogen-bond acceptor. ***P***: positively charged group. ***R***: aromatic ring. ***H***: hydrophobic group.

Table 2. Re-scoring of the docking energies for the selected hits from *Library* 1 and *Library* 2 (ΔG_{bind} = kcal/mol).

Library 1 (non-FDA-approved compounds)			**Library 2 (FDA-approved drugs)**		
Compound	Without phospholipids ΔG_{bind}	With phospholipids ΔG_{bind}	Compound	Without phospholipids ΔG_{bind}	With phospholipids ΔG_{bind}
ZINC58438263	-52.49	-70.02	**Posaconazole**	-59.84	-104.39
ZINC12986242	-46.71	-59.54	**Cepharanthine**	-53.79	-40.41
ZINC06530230	-44.86	-50.16	**Indinavir**	-53.76	-58.04
ZINC07001403	-42.20	-70.48	**Nefazodone**	-46.31	-66.65
ZINC12756822	-40.36	-67.09	**Lapatinib**	-45.73	-19.26
ZINC12430014	-38.22	-77.04	**Suvorexant**	-39.55	-39.03
ZINC33126270	-35.82	-47.73	**Pantoprazole**	-30.72	-42.62
ZINC12890205	-32.04	-36.62	**Pyritinol**	-25.42	-37.32
ZINC64590918	-28.47	-51.42	**Amitraz**	-24.10	-30.02
ZINC24739924	-22.42	-39.93	**Ceforanide**	-20.68	-23.29

Compounds in bold were evaluated experimentally, upon commercial availability.